

A spatiotemporally separated framework for reconstructing the source of atmospheric radionuclide releases

Yuhan Xu¹, Sheng Fang^{1,*}, Xinwen Dong¹, Shuhan Zhuang¹

¹Institute of Nuclear and New Energy Technology, Collaborative Innovation Centre of Advanced Nuclear Energy Technology, Key Laboratory of Advanced Reactor Engineering and Safety of Ministry of Education, Tsinghua University, Beijing 100084, China

*Correspondence to: Sheng Fang (fangsheng@tsinghua.edu.cn)

Abstract. Determining the source location and release rate are critical tasks in assessing the environmental consequences of atmospheric radionuclide releases, but remain challenging because of the huge multi-dimensional solution space. We propose a spatiotemporally separated two-step framework that reduces the dimension of the solution space in each step and improves the source reconstruction accuracy. The separation process applies a temporal sliding-window average filter to the observations, thereby reducing the influence of temporal variations in the release rate on the observations and ensuring that the features of the filtered data are dominated by the source location. A machine learning model is trained to link these features to the source location, enabling independent source location estimations. The release rate is then determined using projected alternating minimization with the L1-norm and total variation regularization algorithm. This method is validated against the local-scale SCK-CEN ⁴¹Ar field experiment and the first release of the continental-scale European Tracer Experiment, for which the lowest relative source location errors are 0.60% and 0.20%, respectively. This presents higher accuracy and a smaller uncertainty range than the correlation-based and Bayesian methods in estimating the source location. The temporal variations in release rates are accurately reconstructed, and the mean relative errors of the total release are 65.09% and 72.14% lower than the Bayesian method for the SCK-CEN experiment and European Tracer Experiment, respectively. A sensitivity study demonstrates the robustness of the proposed method to different hyperparameters. With an appropriate site layout, low error levels can be achieved from only a single observation site or under meteorological errors.

1. Introduction

Atmospheric radionuclide release is a major environmental concern of the nuclear industry, including nuclear energy and its heat applications, isotope production, and the post-processing of radioactive waste. Such releases occurred after the Chernobyl nuclear accident (Anspaugh et al., 1988) and the Fukushima nuclear explosion (Katata et al., 2012), with partially known source information, i.e. the location. Recently, there have been several atmospheric radionuclide leaks from unknown sources, such as the 2017 ¹⁰⁶Ru leakage (Masson et al., 2019) and the 2020 ^{134/137}Cs detection in northern Europe (Ingremeau and Saunier, 2022), which have raised global concerns regarding the subsequent hazard to public health. Identification of source

30 information in these events is critical for the safe operation of nuclear facilities, consequence assessment, and emergency
31 response.

32 During these events, source data often cannot be directly measured or determined because of the lack of information on the
33 source of the leak. Instead, source information can only be reconstructed through inversion methods, which identify the optimal
34 solution by comparing the environmental observations with atmospheric dispersion simulations using different estimates of
35 the source location and release rate. Such reconstructions simultaneously identify the source location and release rate because
36 the observations are intuitively determined by both parameters. In this case, the reconstruction searches for a solution over a
37 large multi-dimensional space, where the dimension is the sum of the number of space coordinates and the length of the
38 estimated release window. Therefore, the inversion is weakly constrained and can become ill-posed in the case of
39 spatiotemporally limited observations and uncertainties in the atmospheric dispersion models. Unfortunately, this is quite often
40 the case for atmospheric radionuclide releases.

41 To reduce the problem of ill-posedness, most previous studies have attempted to constrain the reconstruction by imposing
42 assumptions on the model–observation discrepancies or release characteristics. Assumptions on model–observation
43 discrepancies are widely used in Bayesian methods to simultaneously reconstruct the posterior distributions of spatiotemporal
44 source parameters (De Meutter et al., 2021; Meutter and Hoffman, 2020; Xue et al., 2017a). This assumes that the model–
45 observation discrepancies follow a certain statistical distribution (i.e. the likelihood of Bayesian methods), with the normal
46 (Eslinger and Schrom, 2016; Guo et al., 2009; Keats et al., 2007, 2010; Rajaona et al., 2015; Xue et al., 2017a, b; Yee, 2017;
47 Yee et al., 2008; Zhao et al., 2021) and log-normal (Chow et al., 2008; Dumont Le Brazidec et al., 2020; KIM et al., 2011;
48 Monache et al., 2008; Saunier et al., 2019; Senocak, 2010; Senocak et al., 2008) distributions being two popular choices. Other
49 candidates include the t-distribution (with degrees of freedom ranging from 3–10), Cauchy distribution, and log-Cauchy
50 distribution, all of which were compared against the normal and log-normal distributions in terms of reconstructing the source
51 parameters of the Prairie Grass field experiment (Wang et al., 2017). The results demonstrate that the likelihoods are sensitive
52 to both the dataset and the target source parameters. Several studies have constructed the likelihood based on multiple metrics
53 that measure the model–observation discrepancies in an attempt to better constrain the solution (Lucas et al., 2017; Jensen et
54 al., 2019). More sophisticated methods involve the use of different statistical distributions for the likelihoods of non-detections
55 and detections (De Meutter et al., 2021; Meutter and Hoffman, 2020). Recent studies have suggested the use of log-based
56 distributions and tailored parameterization of the covariance matrix as a means of better quantifying the uncertainties in the
57 reconstruction (Dumont Le Brazidec et al., 2021). These Bayesian methods have been applied to real atmospheric radionuclide
58 releases, such as the 2017 ^{106}Ru event, and have provided important insights into the source and release process (Dumont Le
59 Brazidec et al., 2020; Saunier et al., 2019; Dumont Le Brazidec et al., 2021; De Meutter et al., 2021). However, these studies
60 have also revealed that the likelihood in Bayesian methods must be exquisitely designed and parameterized to achieve
61 satisfactory spatiotemporal source reconstruction (Dumont Le Brazidec et al., 2021; Wang et al., 2017). With suboptimal
62 design, the reconstruction may exhibit a bimodal posterior distribution (Meutter and Hoffman, 2020), which remains a
63 challenge for robust applications in different scenarios.

64 Assumptions on the release characteristics aim to reduce the dimension of the solution space to 4 or 5, namely the two source
65 location coordinates, the total release, and the release time (or the release start and end time), i.e. an instantaneous release at
66 one time or constant release over a period (Kovalets et al., 2020, 2018; Efthimiou et al., 2018, 2017; Tomas et al., 2021;
67 Andronopoulos and Kovalets, 2021; Ma et al., 2018). Under these assumptions, the correlation-based method exhibits high
68 accuracy for ideal cases under stationary meteorological conditions, such as synthetic simulation experiments (Ma et al., 2018)
69 and wind tunnel experiments (Kovalets et al., 2018; Efthimiou et al., 2017). However, previous studies have also demonstrated
70 that real-world applications may be much more challenging, (Kovalets et al., 2020; Tomas et al., 2021; Andronopoulos and
71 Kovalets, 2021; Becker et al., 2007) because the release usually exhibits temporal variations and may experience non-
72 stationary meteorological fields. The interaction between the time-varying release characteristics and non-stationary
73 meteorological fields is neglected in the instantaneous-release and constant-release assumptions, leading to inaccurate
74 reconstruction.

75 Given the assumption-related reconstruction deviations in complex scenarios, we propose a spatiotemporally separated
76 source reconstruction method that is less dependent on such assumptions. Our approach reduces the complexity of the source
77 reconstruction using the simple fact that the source location is fixed during the atmospheric radionuclide release process. In
78 this case, the spatiotemporal variations of observations are influenced by the time-varying release rate, source location, and
79 meteorology, of which the last variable is generally known. The proposed method reduces the influence of the release rate
80 through a temporal sliding-window average filter, making the filtered observations more sensitive to the source location than
81 to the release rate. After filtering, existing methods based on direct observation–simulation comparisons may be unable to
82 locate the source. Thus, the response features of the filtered observations are extracted and mapped to the source location by
83 training a data-driven machine learning model using the extreme gradient boosting (XGBoost) algorithm (Chen and Guestrin,
84 2016). To fully capture the response features at each observation site, tailored time- and frequency-domain features are
85 designed and optimized using the feature selection technique of XGBoost. Using this optimized model, the source location is
86 estimated based on the filtered observations. Once the source location has been retrieved, the non-constant release rate is
87 determined using the Projected Alternating MINimization with L1-norm and Total variation regularization (PAMILT)
88 algorithm (Fang et al., 2022), which is robust to model uncertainties. The sequential spatiotemporal reconstruction reduces the
89 dimension of the solution space at each step, which helps to improve the accuracy and reliability of the reconstruction.

90 The proposed method is validated using the data from multi-scales field experiments, namely the local-scale SCK-CEN ^{41}Ar
91 experiment (Rojas-Palma et al., 2004), and the first release of the continental scale European Tracer Experiment (ETEX-1)
92 (Nodop et al., 1998), which traced emissions of Perfluoro-Methyl-Cyclo-Hexane (PMCH). The performance of the proposed
93 method is compared with the correlation-based method in terms of source location estimation and the Bayesian method in
94 terms of spatiotemporal accuracy. The sensitivity of the source location estimation to the spatial search range, size of the
95 sliding window, feature type, number and combination of sites, and meteorological errors is also investigated for the SCK-
96 CEN ^{41}Ar experiment.

97 **2. Materials and Methods**

98 **2.1 Source reconstruction models**

99 For an atmospheric radionuclide release, Eq. (1) relates the observations at each observation site to the source parameters:

$$100 \quad \boldsymbol{\mu} = \mathbf{F}(\mathbf{r}, \mathbf{q}) + \boldsymbol{\varepsilon}, \quad (1)$$

101 where $\boldsymbol{\mu} = [\mu_1, \mu_2, \dots, \mu_N]^T \in \mathbb{R}^N$ is an observation vector composed of observations at N sequential time steps, the function
102 \mathbf{F} maps the source parameters to the observations, i.e. an atmospheric dispersion model, \mathbf{r} refers to the source location, $\mathbf{q} \in \mathbb{R}^S$
103 is the temporally varying release rate, and $\boldsymbol{\varepsilon} \in \mathbb{R}^N$ is a vector containing both model and measurement errors.

104 In most source reconstruction models, \mathbf{F} is simplified to the product of \mathbf{q} and a source–receptor matrix \mathbf{A} that depends on
105 the source location:

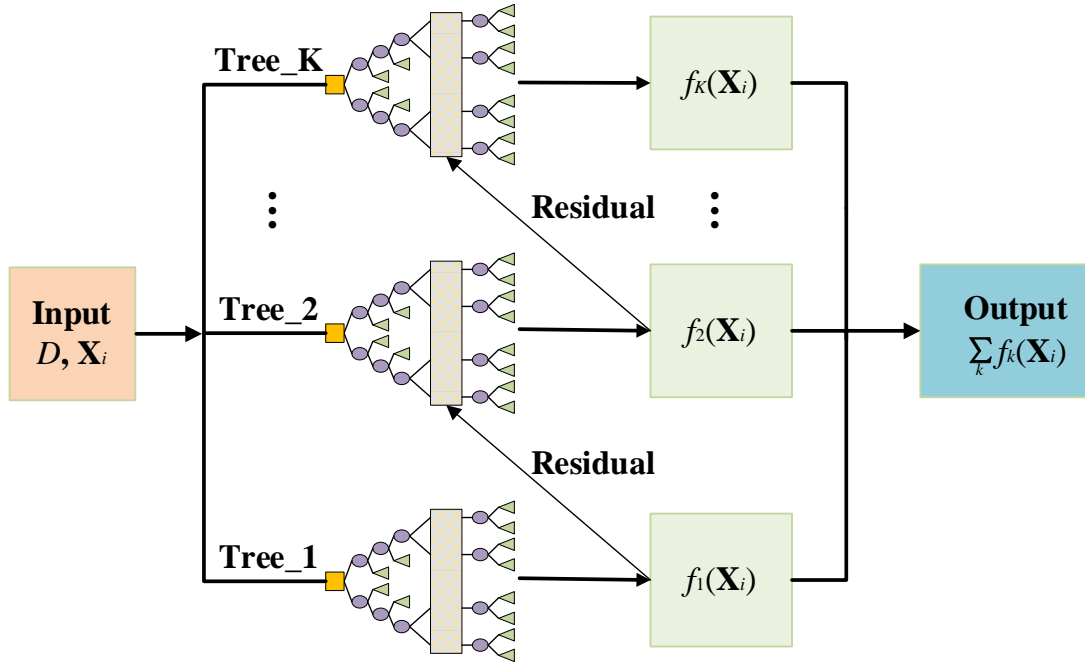
$$106 \quad \boldsymbol{\mu} = \mathbf{A}(\mathbf{r})\mathbf{q} + \boldsymbol{\varepsilon}, \quad (2)$$

107 where $\mathbf{A}(\mathbf{r}) = [A_1(\mathbf{r}), A_2(\mathbf{r}), \dots, A_N(\mathbf{r})]^T \in \mathbb{R}^{N \times S}$ and each row describes the sensitivity of an observation to the release rate
108 \mathbf{q} given the source location \mathbf{r} .

109 **2.2 Observation filtering for spatiotemporally separated reconstruction**

110 A straightforward way to solve Eq. (2) is to simultaneously retrieve the source location and release rate; however, the solution
111 space is huge and difficult to constrain. Several studies have noted that the source location can be retrieved separately without
112 knowledge of the exact release rate, on the condition that the release rate is constant (Efthimiou et al., 2018; Kovalets et al.,
113 2018; Efthimiou et al., 2017; Ma et al., 2018). The key reason is that, in constant-release cases, the relative spatiotemporal
114 distribution of radionuclides is determined by the meteorological conditions and the relative positions between the source and
115 receptors, and the constant release rate only changes the absolute values. Although the release rate may counteract the influence
116 of the meteorological conditions and relative position at a single observation site, it cannot change the whole spatiotemporal
117 distribution at multiple observation sites. Therefore, by analysing the spatiotemporal distribution of radionuclides at multiple
118 observation sites, it is possible to locate the source without knowing the release rate under the constant-release assumption.

119 To provide a more general method, we take advantage of the fact that the source location has been fixed during all known
120 atmospheric radionuclide releases, such as the Chernobyl nuclear accident (Anspaugh et al., 1988), Fukushima nuclear
121 explosion (Katata et al., 2012), and 2017 ^{106}Ru leakage (Masson et al., 2019). With a fixed source location, the release rate and
122 meteorology jointly determine the temporal variations of the observations (Li et al., 2019b). The influence of meteorology can
123 be pre-calculated as the source–receptor sensitivities and subsequently stored in matrix $\mathbf{A}(\mathbf{r})$. By reducing the influence of the
124 release rate, the constant-release case can be approximated and the sensitivity of the observations to the source location can be
125 improved, enabling separate source location and release rate estimations and reducing the solution space at each step. For this
126 purpose, we introduce an operator matrix $\mathbf{P} \in \mathbb{R}^{N \times N}$ to reduce the temporal variations of $\mathbf{A}(\mathbf{r})\mathbf{q}$:



152

153 **Figure 1.** Flowchart of XGBoost for predicting $\hat{\mathbf{f}}_i$ based on decision tree model. The yellow squares are the root nodes within each tree, representing the input features in this paper. The purple ellipses denote the child nodes where the model evaluates input features and make
154 decisions to split the data. The green rectangles depict the leaf nodes and refer to the prediction results. The vertical rectangles abstract the
155 internal splitting processes of the trees, indicating decision-making not explicitly detailed in the diagram.
156

157 XGBoost trains $G(\mathbf{X})$ in Eq. (5) by continuously fitting the residual error until the following objective function is minimized:

$$158 \text{Obj}^{(t)} = \sum_{i=1}^n \left(\mathbf{r}_i - \left(\hat{\mathbf{f}}_i^{(t-1)} + f_t(\mathbf{X}_i) \right) \right)^2 + \sum_{i=1}^t \Omega(f_i), \quad (6)$$

159 where t represents the training of the t -th tree and $\Omega(f_i)$ is the regularization term, given by:

$$160 \Omega(f) = YM + \frac{1}{2} \lambda \sum_{j=1}^M \omega_j^2, \quad (7)$$

161 where M is the number of leaf nodes, ω_j is the leaf node weight for the j -th leaf node, and Y, λ are penalty coefficients. The
162 minimization of Eq. (6) provides a parametric model $G(\mathbf{X})$ that maps the feature ensemble \mathbf{X} extracted from μ_p to the source
163 location \mathbf{r} .

164 To comprehensively evaluate the influence of the source location, both time- and frequency-domain features (as outlined in
165 Table 1) are considered during the training process and mapped to the source location by $G(\mathbf{X})$. Among the time-domain
166 features, the wave rate quantifies the fluctuations of μ_p over time, while the temporal mean and median values are measures
167 of the central tendency of μ_p (Witte and Witte, 2017). The sample entropy measures the complexity of μ_p , with a lower sample
168 entropy indicating greater self-similarity and less randomness in μ_p . The frequency-domain features are calculated based on

169 the fast Fourier transform (FFT). The FFT mean is the mean value of the Fourier coefficients for μ_p and the FFT shape mean
 170 describes the shape of the Fourier coefficients. These quantities are formulated as follows:

$$171 \text{ FFT mean} = \frac{1}{N} \sum_{k=1}^N |\mu_{ik}|, \quad (8)$$

$$172 \text{ FFT shape mean} = \frac{1}{\sum_{k=1}^N |\mu_{ik}|} \sum_{k=1}^N k |\mu_{ik}|, \quad (9)$$

173 where μ_{ik} is the Fourier coefficient and N is the length of μ_p . These features are calculated from the simulated observations at
 174 each site and provided to XGBoost as initial inputs.

175 **Table 1.** Summary of the basic information on the observation series features.

Attribute	Feature	Description
Time domain	Wave rate	Difference between 90-th and 10-th quantile of normalized observation series
	Mean	Temporal mean value of observation series
	Median	Temporal median value of observation series
Frequency domain	Sample entropy	Complexity of observation series
	FFT mean	Amplitude of power spectral density by FFT
	FFT shape mean	Shape of power spectral density by FFT

176 2.4 Release rate estimation

177 Once the source location has been retrieved, many existing methods can be used to inversely estimate the release rate. In this
 178 study, we choose the recently developed PAMILT method (Fang et al., 2022) because it can correct the intrinsic model errors
 179 of the release rate estimation and accurately retrieve the temporal variations in the release rates.

180 2.5 Numerical implementation

181 2.5.1 Pre-screening of potential source locations

182 To reduce the computational cost and remove low-quality samples, the search range for the source location is pre-screened by
 183 evaluating the correlation coefficients between the observations and atmospheric dispersion model simulations, where the
 184 candidate source locations are randomly sampled in the considered calculation domain. Because the release rate is unknown,
 185 it is assumed to be 1 for all simulations. Source locations corresponding to the highest 40% of correlation coefficients are
 186 selected as the search range of the subsequent refined source location estimation using XGBoost.

187 2.5.2 Samples for training XGBoost

188 The samples for training $G(\mathbf{X})$ in Eq. (5) are generated based on the simulations described in Sect. 2.5.1, and the source
189 locations of these simulations are within the search range determined according to Sect. 2.5.1. The simulation data are scaled
190 by a constant factor (the ratio between the median value of all observations and that of the simulations using a unit release
191 rate), which ensures that the simulations and observations have the same order of magnitude. Gaussian noise is added to the
192 simulation data to simulate the statistical fluctuations of the measurements. The simulations between the first and last data
193 points above the noise level are filtered by a temporal sliding-window average filter with a window size of 5, yielding samples
194 for feature extraction as described in Sect. 2.3.

195 2.5.3 Automatic optimization of XGBoost model

196 The XGBoost model for source location estimation is automatically optimized with respect to the hyperparameters and feature
197 selection. Specifically, the Bayesian optimization algorithm is used to optimize the hyperparameters by minimizing the
198 following generalization coefficient (GC) defined under the five-fold cross-validation framework:

$$199 \text{GC} = (1 - \text{MCV})^2 + \text{Var}(R_k^2), \quad (10)$$

$$200 \text{MCV} = \frac{1}{5} \sum_k R_k^2, \quad (11)$$

201 where R_k^2 is the goodness of fit and k is the index of each fold ($k = 1, 2, \dots, 5$). MCV is the mean cross-validation score R_k^2
202 among the five folds and $\text{Var}(R_k^2)$ measures the variance of R_k^2 . This function aims to balance the average and the variance of
203 R_k^2 , thus enhancing the generalization ability of the XGBoost model. In this study, the optimized hyperparameters include
204 *max_depth* (maximum depth of a decision tree), *learning_rate* (step size shrinkage when updating), *n_estimators* (number of
205 decision trees), *min_child_weight* (minimum sum of sample weight of a child node), *subsample* (subsample ratio of the training
206 samples), *colsample_bytree* (subsample ratio of columns when constructing a decision tree), *reg_lambda* (L2 regularization
207 term on weights), and *gamma* (minimum loss reduction required to split the decision tree).

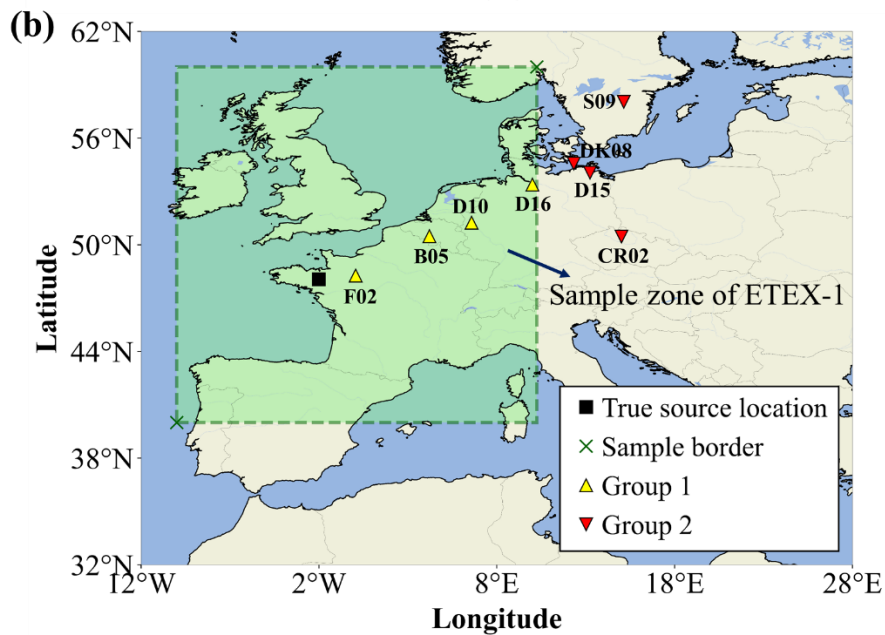
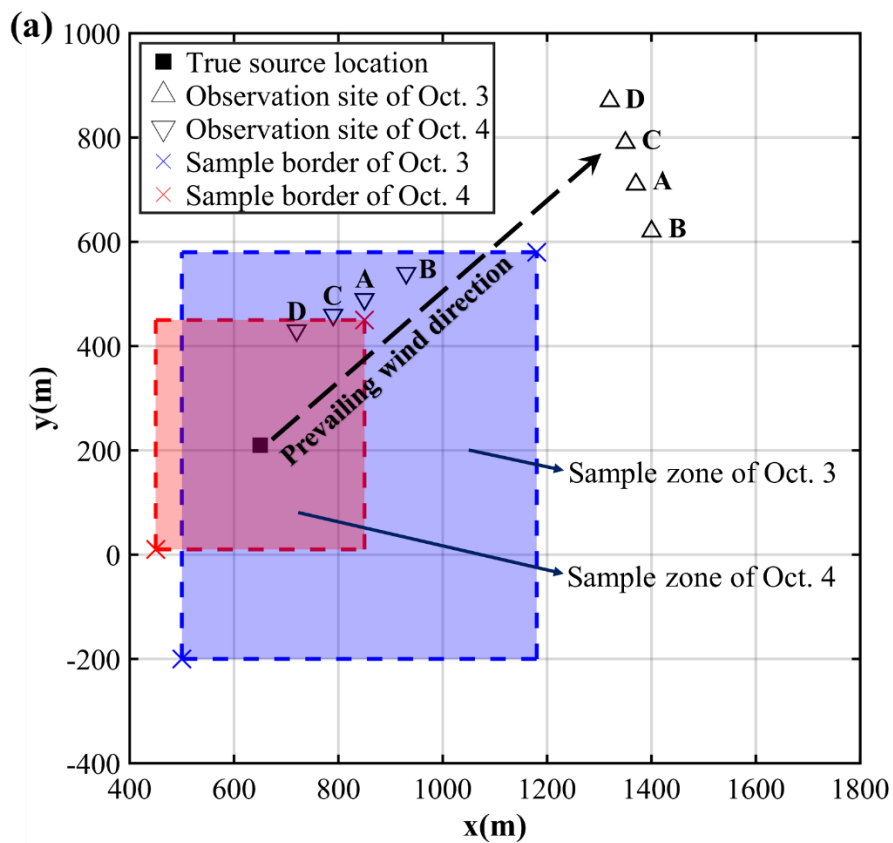
208 The initial input features (Table 1) are optimized through a feature selection step, where MCV serves as the selection
209 criterion. The selection is implemented by recursively removing the feature with the least importance, and reassessing the
210 MCV based on cross-validation (Akhtar et al., 2019). Initially, an XGBoost model is trained with all features, and the
211 importance of each feature is assessed based on its contribution to the model accuracy. The feature with the least importance
212 is removed and the XGBoost model is retrained using the remaining features. The feature importance and MCV are updated
213 accordingly and another feature is removed. This iterative process continues until the optimal number of features is identified,
214 corresponding to the highest MCV achieved during the process. The overall flowchart of the proposed spatiotemporally
215 separated source reconstruction model is shown in Fig. S1.

216 2.6 Validation case

217 2.6.1 Field experiments

218 The proposed methodology was validated against the observations of the SCK-CEN ^{41}Ar and ETEX-1 field experiments. The
219 SCK-CEN ^{41}Ar experiment was carried out at the BR1 research reactor in Mol, Belgium, in October 2001 as a collaboration
220 between NKS and the Belgian Nuclear Research Centre (SCK-CEN) (Rojas-Palma et al., 2004). The major part of the
221 experiment was conducted on 3–4 October, during which time ^{41}Ar was emitted from a 60-m stack with a release rate of
222 approximately $1.5 \times 10^{11} \text{ Bq h}^{-1}$. Meteorological data such as wind speed and direction were provided by the on-site weather
223 mast. For most of the experimental period, the atmospheric stability was neutral, and the wind was blowing from the southwest.
224 As illustrated in Fig. 2(a), the source coordinates were (650 m, 210 m). The 60-s-average ground-level fluence rates were
225 continuously collected by an array of NaI (Tl) gamma detectors, with different observation sites used on the two days. To
226 convert the measured fluence rates to gamma dose rates (mSv/h), we used the ^{41}Ar parameters of a previous study (Li et al.,
227 2019a): $E_\gamma = 1.2938 \text{ MeV}$, $f^n(E_\gamma) = 0.9921$, $\mu_a = 2.05 \times 10^{-3} \text{ m}^{-1}$, and $\omega = 7.3516 \times 10^{-1} \text{ Sv Gy}^{-1}$. More details of
228 these measurements can be found in (Rojas-Palma et al., 2004).

229 The ETEX-1 experiment took place at Monterfil in Brittany, France, on 23 October 1994 (Nodop et al., 1998). During
230 ETEX-1, a total of 340 kg of PMCH was released into the atmosphere on 23 October 1994 at 16:00:00 UTC and 24 October
231 1994 at 03:50:00 UTC. As illustrated in Fig. 2(b), the source coordinates were (-2.0083°E, 48.058°N). A total of 3104 available
232 observations (3-h-averaged concentrations) were collected at 168 ground sites. ETEX-1 has been widely used as a validation
233 scenario for reconstructing atmospheric radionuclide releases (Ulimoen and Klein, 2023; Tomas et al., 2021). The candidate
234 source locations are uniformly sampled from the green shaded zone. We choose two groups of observation sites: the first
235 comprises four sites (i.e. B05, D10, D16, F02) randomly selected from the sites within the sample zone (Group 1, with a total
236 of 92 available observations), and the second involves four sites (i.e. CR02, D15, DK08, S09) randomly selected from the sites
237 beyond the sample zone boundaries (Group 2, with a total of 90 available observations). Compared with the SCK-CEN ^{41}Ar
238 experiment, the ETEX-1 observations exhibit temporal sparsity, lower temporal resolution, and increased complexity in
239 meteorological conditions.



240

241

Figure 2. Release location and observation sites of two field experiments. (a) SCK-CEN ^{41}Ar experiment. The map was created based on

242 the relative positions of the release source and observation sites (Drews et al., 2002). The coordinates of the sample border are (500 m, -200
243 m) and (1180 m, 580 m) on Oct. 3, and (450 m, 10 m) and (850 m, 450 m) on Oct. 4. This figure was plotted using MATLAB 2016b, rather
244 than created by a map provider; (b) ETEX-1 experiment. The map was created based on the real longitudes and latitudes of the release source
245 and observation sites (Nodop et al., 1998). The coordinates of the sample border are (10°W, 40°N) and (10°E, 60°N). This figure was plotted
246 using the cartopy function of Python, rather than created by a map provider.

247 **2.6.2 Simulation settings of atmospheric dispersion model**

248 For the SCK-CEN ⁴¹Ar field experiment, the Risø Mesoscale PUFF (RIMPUFF) model was employed to simulate the
249 dispersion of radionuclides and calculate the dose rates at each observation site (Thykier-Nielsen et al., 1999). The simulations
250 used on-site measured meteorological data and the modified Karlsruhe–Jülich diffusion coefficients. The calculation domain
251 measured 1800 m×1800 m and the grid resolution was 10 m×10 m. The release height of ⁴¹Ar was assumed to be 60 m. Other
252 RIMPUFF calculation settings followed those of a previous study (Li et al., 2019a), and have been validated against the
253 observations. To establish the datasets for the XGBoost model, 2000 simulations and 1000 simulations with different source
254 locations were performed by RIMPUFF for the experiments on Oct. 3 and Oct. 4, respectively. Candidate source locations
255 were randomly sampled from the shaded zones in Fig. 2(a), which were determined according to the positions of the
256 observation sites and the upwind direction. Each simulation, along with its corresponding source location, forms one
257 sample. As described in Sect. 2.5.1, we calculated the correlation coefficient for each sample and preserved the 40% of samples
258 with the highest 40% of correlation coefficients (i.e. 800 samples for Oct. 3 and 400 samples for Oct. 4). The constant factors
259 mentioned in Sect. 2.5.2 are 1.53×10^{11} and 1.48×10^{11} for Oct. 3 and Oct. 4, respectively.

260 For the ETEX-1 experiment, the FLExible PARTicle (FLEXPART) model (version 10.4) was applied to simulate the
261 dispersion of PMCH (Pisso et al., 2019). The meteorological data were obtained from the United States National Centers of
262 Environmental Prediction Climate Forecast System Reanalysis, and have a spatial resolution of $0.5^\circ \times 0.5^\circ$ and time resolution
263 of 6 h. To rapidly establish the relationship between the varying source locations and the observations, 182 backward
264 simulations were performed using FLEXPART with a time interval of 3 h, grid size of $0.25^\circ \times 0.25^\circ$, and 8 vertical levels (from
265 100–50000 m). Only the lowest model output layer was used for source reconstruction. Candidate source locations were
266 uniformly sampled from the shaded zone in Fig. 2(b), resulting in a total of 6561 source locations. As described in Sect. 2.5.1,
267 2624 candidate source locations were preserved following the pre-screening step. The constant factors mentioned in Sect. 2.5.2
268 are 5.60×10^{12} and 2.86×10^{13} for Group 1 and Group 2, respectively.

269 **2.7 Sensitivity study**

270 (1) Search range

271 The search range is controlled by the pre-screening threshold, which is the top proportion of the correlation coefficients in
272 the pre-screening step. Specifically, we use source locations corresponding to the highest 20%, 40%, 50%, 60%, 80%, and
273 100% of correlation coefficients to define the search ranges, with a lower proportion indicating a narrower and more focused
274 search area.

275 (2) Size of the sliding window

276 Temporal filtering with different sliding-window sizes is applied to separate the source location estimation from the release
277 rate estimation. In this study, the size of the sliding window ranges from 3–10. With these filtered data, the XGBoost model is
278 trained using the same pattern for the source location estimation.

279 (3) Feature type

280 The XGBoost model is trained using only time-domain features and only frequency-domain features to investigate the
281 influence of these features on the source location estimation. The performance of the time-feature-only and frequency-feature-
282 only models is compared with the all-features result.

283 (4) Number and combination of observation sites

284 The XGBoost model is trained and applied to the source location estimation with different numbers of observation sites,
285 namely a single site, two sites, and three sites. For the two- and three-site cases, the model is trained using different
286 combinations of sites and the source location is estimated accordingly.

287 (5) Meteorological errors

288 Meteorological errors are important uncertainties in source reconstruction, especially the random errors in the wind field
289 (Mekhaimr and Abdel Wahab, 2019). To simulate such uncertainties, a stochastic perturbation of $\pm 10\%$ is introduced to the
290 observed wind speeds in the x and y components, and a ± 1 stability class perturbation is applied to the stability parameters
291 (e.g., from C to B or D). For both days, 50 meteorological groups are generated based on these random perturbations.

292 In all the sensitivity tests, the source location is estimated 50 times with randomly initialized hyperparameters to demonstrate
293 the uncertainty range of the proposed method under different circumstances. The performance of source location estimation is
294 compared quantitatively using the metrics specified in Sect. 2.8.3.

295 **2.8 Performance evaluation**

296 **2.8.1 Observation filtering**

297 The feasibility of filtering is demonstrated using both the synthetic and real observations of the SCK-CEN ^{41}Ar experiment
298 and the real observations of the ETEX-1 experiment. The synthetic observations are generated by a simulation using a synthetic
299 temporally varying release profile with sharp increase, stable, and gradual decrease phases (as illustrated in Fig. S2), which is
300 typical for an atmospheric radionuclide release (Davoine and Bocquet, 2007). Because several temporal observations are
301 missing at some observation sites, we only choose observations sampled between 24 October 1994 09:00:00 UTC and 26
302 October 1994 03:00:00 UTC for the source location estimation. The simulations corresponding to the synthetic and real
303 observations should first be processed following the procedure described in Sect. 2.5.2. The filtering performance is evaluated
304 by comparing the simulation–observation differences before and after the filtering step. Several statistical metrics can be used
305 to quantify this difference, including the normalized mean square error (NMSE), Pearson’s correlation coefficient (PCC), and
306 the fraction of predictions within a factor of 2 and 5 of the observations (FAC 2 and FAC 5, respectively) (Chang and Hanna,

307 2004).

308 **2.8.2 Optimization of the XGBoost model**

309 The hyperparameters are optimized with respect to the GC in Eq. (10) and the features are optimized with respect to the MCV
310 in Eq. (11). Larger values of MCV and smaller values of GC indicate better optimization performance. In addition, the
311 importance of each feature to the XGBoost training is evaluated with the built-in *feature importance* measure of the XGBoost
312 model.

313 **2.8.3 Source reconstruction**

314 The relative errors in the source location (δ_r) and total release (δ_Q) are calculated to evaluate the source reconstruction accuracy:

$$315 \delta_r = \frac{|\mathbf{r}_{true} - \mathbf{r}_{est}|}{L_D} \times 100\% , \quad (12)$$

$$316 \delta_Q = \frac{Q_{true} - Q_{est}}{Q_{true}} \times 100\% , \quad (13)$$

317 where \mathbf{r}_{true} and Q_{true} refer to the real source location and total release of the field experiment and \mathbf{r}_{est} and Q_{est} are the
318 estimated location and total release, respectively. L_D represents the range of the source domain, which is the distance between
319 the lower and upper borders of the sampled zone (Fig. 2). The values of \mathbf{r}_{true} , L_D , and Q_{true} are listed in Table 2. In addition
320 to the total release, the reconstructed release rates are also compared with the true temporal release profile.

321 **Table 2.** Parameter settings of field experiments.

Experiment	Case	Parameters		
		\mathbf{r}_{true}	L_D	Q_{true}
SCK-CEN ⁴¹ Ar	Oct. 3	(650 m, 210 m)	1034.8 m	423.10 GBq
	Oct. 4	(650 m, 210 m)	565.7 m	1045.09 GBq
ETEX-1	Group 1	(2.0083°W, 48.058°N)	2620.5 km	340 kg
	Group 2	(2.0083°W, 48.058°N)	2620.5 km	340 kg

322 **2.8.4 Comparison with the Bayesian method**

323 The proposed method is compared with the popular Bayesian method based on the SCK-CEN ⁴¹Ar and ETEX-1 experiments,
324 with the same search range used for locating the source in both methods (Fig. 2). The Bayesian method is augmented with an
325 in-loop inversion of the release rate at each iteration of the Markov chain Monte Carlo sampling. The prior distribution of the
326 Bayesian method is a uniform distribution and the likelihood is a log-Cauchy distribution. More detailed information is

327 presented in Supplementary Note S1.

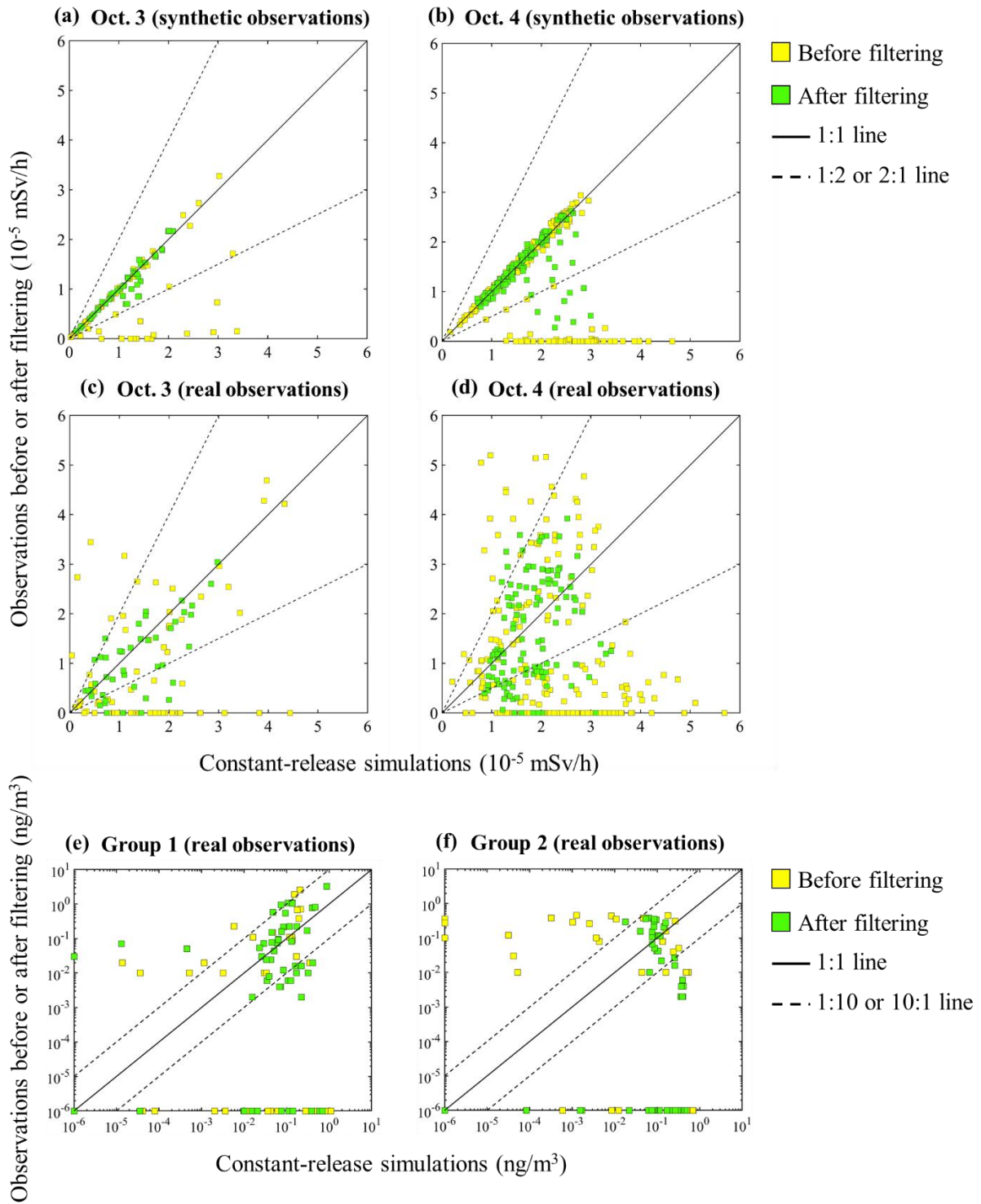
328 **2.8.5 Uncertainty range**

329 The uncertainty ranges are calculated and compared for the correlation-based method, the Bayesian method, and the proposed
330 method. For the correlation-based method, the uncertainty range is calculated using the source locations with the top-50
331 correlation coefficients. For the proposed method, the uncertainty range is calculated from 50 Monte Carlo runs with randomly
332 initialized hyperparameters. The Bayesian method provides the uncertainty range directly through the posterior distribution.
333 For consistency with the other two methods, the results with the top-50 frequencies are selected for the comparison.

334 **3. Results and Discussion**

335 **3.1 Filtering performance**

336 Figure S3 displays the original and filtered observations at different observation sites for both days. The results demonstrate
337 that the peak values have been smoothed out and the long-term trends are preserved to a large degree. Figure 3 compares the
338 filtering performance for both the synthetic and real observations, where the constant-release simulations are plotted against
339 the observations before and after filtering. For the synthetic observations, the filtered data are more concentrated along the 1:1
340 line for both days, and all filtered data fall within the 2-fold lines for Oct. 3. For the real observations, the dots before filtering
341 in Fig. 3 have a dispersed distribution for both Oct. 3 and Oct. 4, indicating limited correlations with the simulations. After
342 filtering, the dots are more concentrated towards the 1:1 line for both the SCK-CEN ⁴¹Ar and ETEX-1 experiments. These
343 phenomena indicate a noticeably increased agreement between the filtered observations and the constant-release simulations.



344

345

Figure 3. Scatter plots of the original (yellow squares) and filtered (green squares) observations versus the constant-release simulation results.

346 SCK-CEN ^{41}Ar experiment: (a) Oct. 3 (synthetic observations); (b) Oct. 4 (synthetic observations); (c) Oct. 3 (real observations); (d) Oct. 4
 347 (real observations); ETEX-1 experiment: (e) Group 1 (real observations); (f) Group 2 (real observations).

348 Table 3 quantitatively compares the results presented in Fig. 3. For each case, all metrics are greatly improved after filtering,
 349 confirming the better agreement between the filtered observations and the constant-release simulations. The improved
 350 agreement indicates that the filtering step significantly reduces the influence of temporal variations in release rates across the
 351 observations. The filtering performs better with the synthetic observations than with the real observations because the synthetic
 352 observations are free of measurement errors. The filtering process produces a better effect with the SCK-CEN ^{41}Ar experiment
 353 than with the ETEX-1 experiment, owing to the sparser observations in the ETEX-1 experiment (Fig. S3).

354 **Table 3.** Quantitative metrics for the filtering validation.

Experiment	Case		NMSE	PCC	FAC2	FAC5	
SCK-CEN ^{41}Ar	Oct. 3 (synthetic observations)	Before filtering	0.6970	0.5315	0.7647	0.8235	
		After filtering	0.0239	0.9514	1	1	
	Oct. 4 (synthetic observations)	Before filtering	0.9290	-0.0267	0.7292	0.7292	
		After filtering	0.0956	0.6179	0.9412	0.9779	
	Oct. 3 (real observations)	Before filtering	1.4437	0.3572	0.3824	0.5147	
		After filtering	0.2730	0.6976	0.7273	0.8864	
	Oct. 4 (real observations)	Before filtering	1.9290	-0.2099	0.3073	0.4948	
		After filtering	0.3668	0.2802	0.6552	0.9310	
	ETEX-1	Group 1 (real observations)	Before filtering	10.9936	0.3414	0.1000	0.2167
			After filtering	6.6769	0.5145	0.2500	0.3667
		Group 2 (real observations)	Before filtering	5.8705	-0.2824	0.0667	0.1167
			After filtering	4.9799	-0.2695	0.1167	0.2500

355 3.2 Optimization of XGBoost model

356 3.2.1 Hyperparameters

357 Table S1 summarizes the optimal hyperparameters and corresponding GCs used for source location estimation in this study;
 358 Tables S2–S5 includes all the optimal hyperparameters used in the 50 runs of the SCK-CEN ^{41}Ar and ETEX-1 experiments.
 359 The optimal GCs of the SCK-CEN ^{41}Ar experiment are smaller than those of the ETEX-1 experiment, indicating better fitting
 360 performance. This is because the sparse observations of the ETEX-1 experiment (Fig. S3) are more sensitive to the added

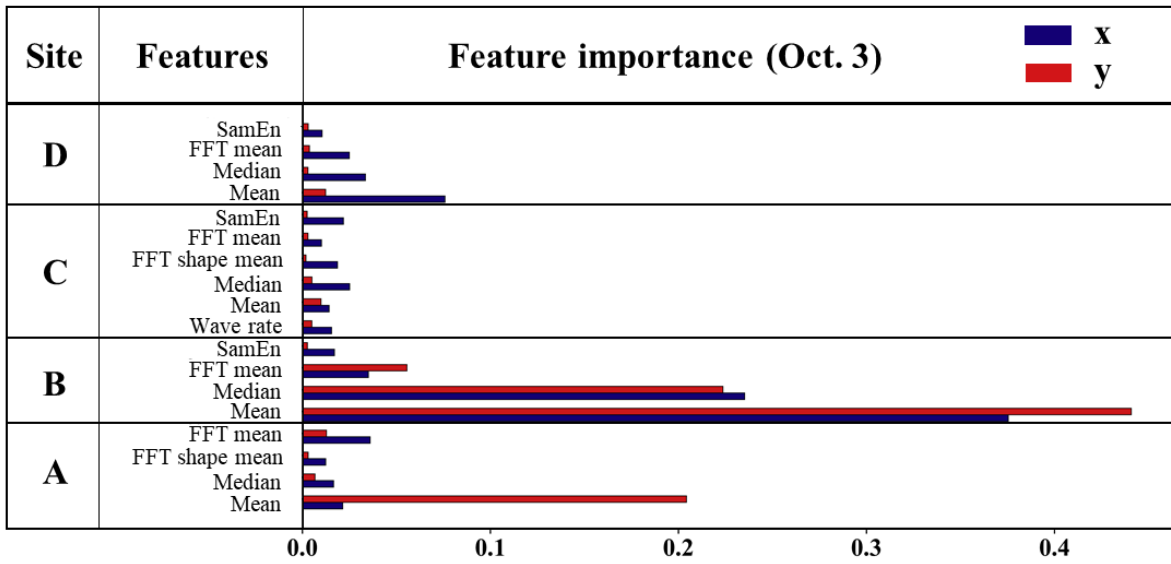
361 Gaussian noise (see Sect. 2.5.2).

362 **3.2.2 Feature selection**

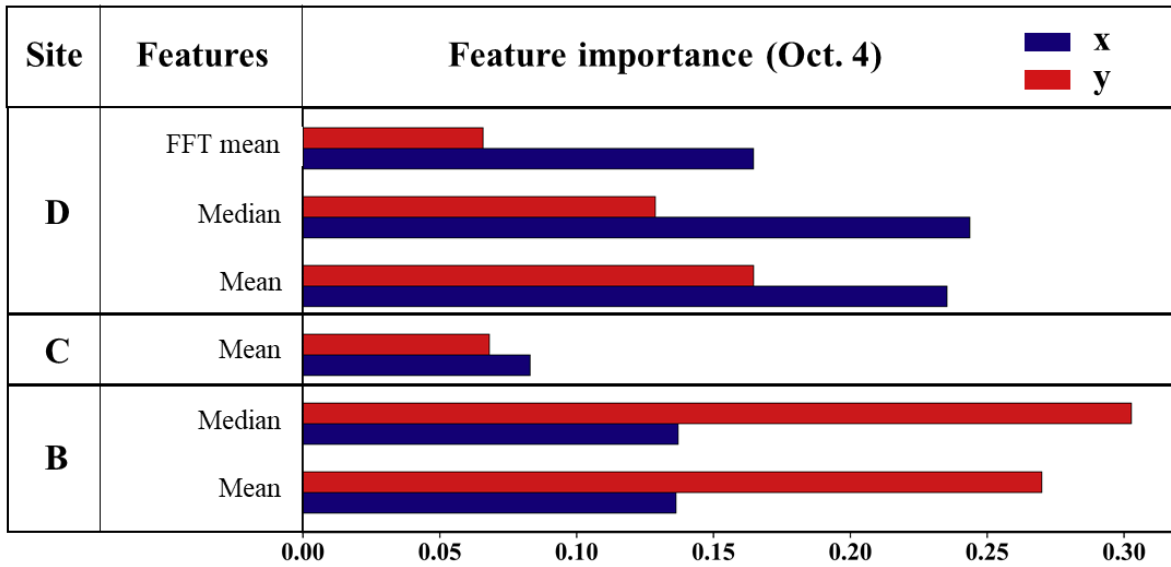
363 Figure 4 compares the importance of the selected features at each site for the two experiments. The time-domain features are
364 dominant for both days in the SCK-CEN ⁴¹Ar experiment (Fig. 4a and 4b). For Oct. 3, Site B is the most important, possibly
365 because it is farthest away in the crosswind direction. For Oct. 4, the four sites provide redundant feature information, and
366 many features are removed. This is because the distribution of observation sites is almost parallel to the wind direction on this
367 day. According to Fig. S3(b), the measurements from Sites A and B have a high correlation, thus leading to the removal of
368 features from Site A on Oct. 4. In summary, the feature selection process adapts XGBoost to different application scenarios.
369 Figure S4(a) and S4(b) shows the variations in MCV with the number of features for the x and y coordinates. The MCV first
370 increases with the number of features, and then decreases slightly after reaching the maximum. The optimal number of features
371 for Oct. 4 is noticeably smaller than for Oct. 3. In addition, the selected features for Oct. 3 involve all four sites, whereas those
372 for Oct. 4 involve three sites. The reduced features and site numbers indicate a high level of redundancy in the observations
373 acquired on Oct. 4. This is because the observation sites are parallel to the downwind direction and provide similar location
374 information in the crosswind direction.

375 For the ETEX-1 experiment, Fig. 4c and d shows that the features of Group1 and Group2 are largely preserved after the
376 feature selection process (only one feature is removed for each case), indicating less redundancy than that in the SCK-CEN
377 ⁴¹Ar experiment. The time-domain features are dominant, but the frequency-domain features at some sites (e.g. D16 and S09)
378 also play important roles. The MCVs of the ETEX-1 experiment have similar variation trends as those for the SCK-CEN ⁴¹Ar
379 experiment (Fig. S4c and S4d).

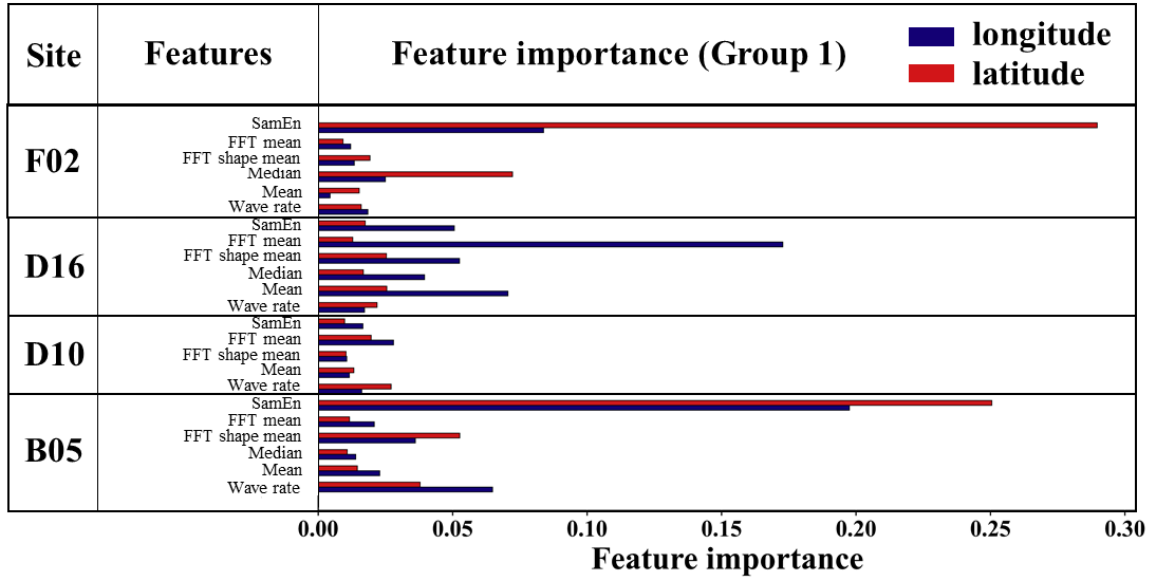
(a)



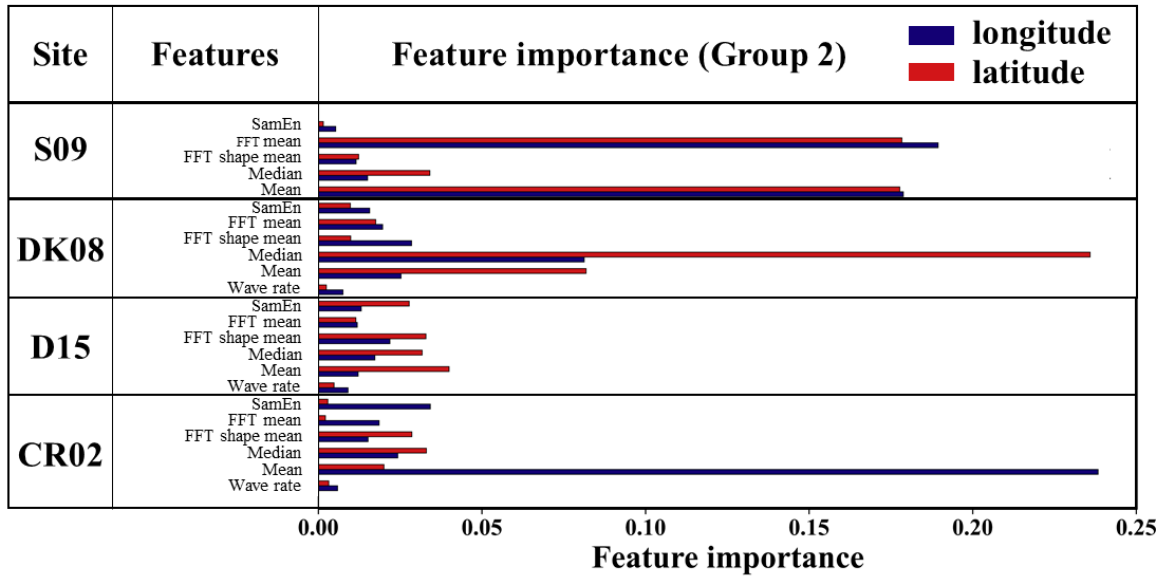
(b)



(c)



(d)



381

382 **Figure 4.** Feature importance of SCK-CEN ^{41}Ar experiment: (a) Oct. 3; (b) Oct. 4; and ETEX-1 experiment: (c) Group 1; (d) Group 2.

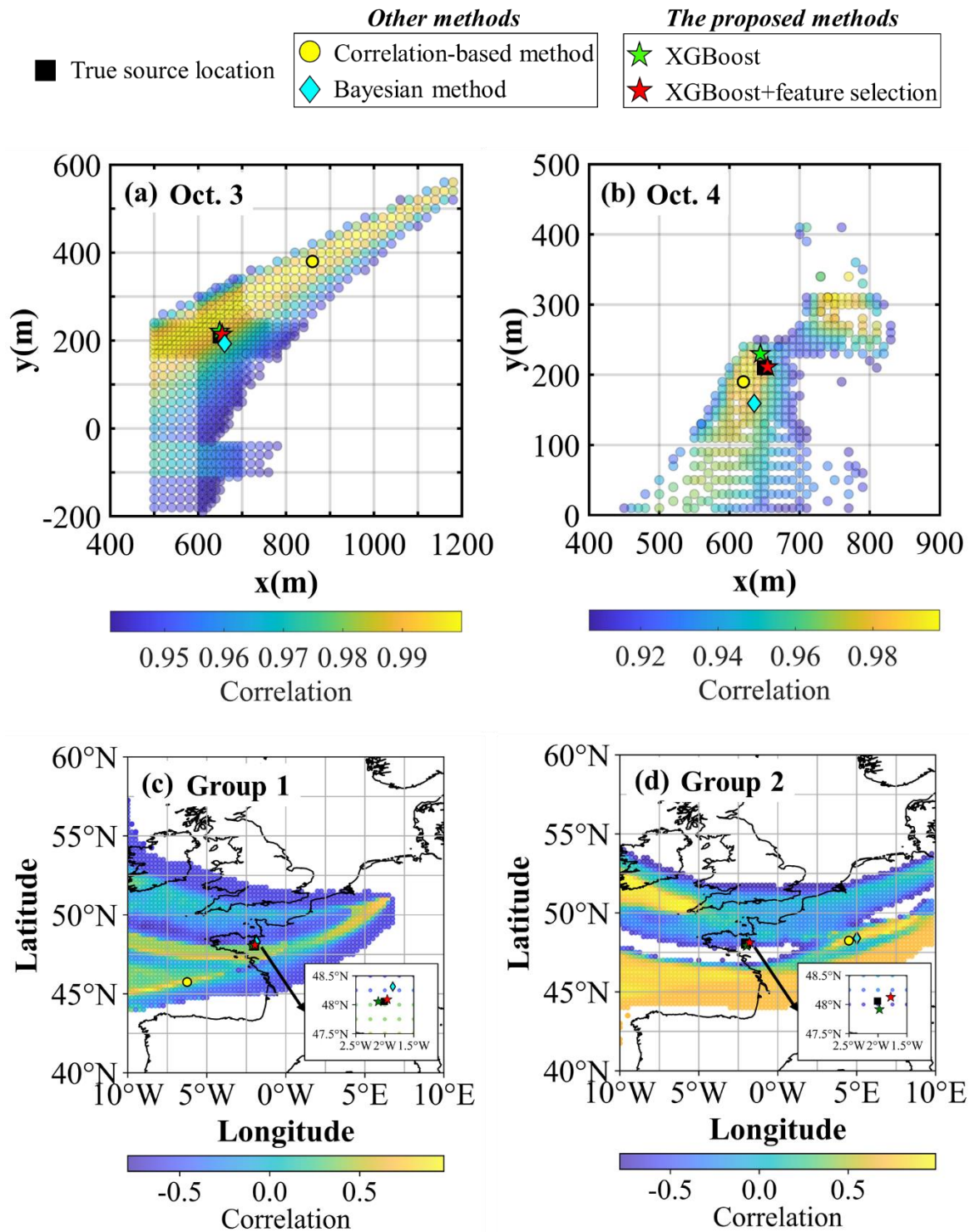
383 **3.3 Source reconstruction**

384 **3.3.1 Source locations**

385 Figure 5 compares the best-estimated source locations of the correlation-based method, the Bayesian method, and the proposed
386 method with the ground truth. The pre-screening zone covers the true source location for both days, but the areas with the

387 highest correlation coefficients are still too large for the point source to be accurately located. The locations with the maximum
388 correlation exhibit errors of 270.19 m and 36.06 m for Oct. 3 and Oct. 4, respectively, indicating that the correlation-based
389 method may produce biased results in the case of non-constant releases. The Bayesian method estimates the location with
390 errors of 19.62 m and 52.81 m for Oct. 3 and Oct. 4, respectively. In comparison, the proposed method achieves the best
391 performance. The estimates without feature selection are only 10.65 m (Oct. 3) and 20.62 m (Oct. 4) away from the true
392 locations. Feature selection further reduces these errors to 6.19 m (Oct. 3, a relative error of 0.60%) and 4.52 m (Oct. 4, a
393 relative error of 0.80%), which are below the grid size ($10\text{ m}\times 10\text{ m}$) of the atmospheric dispersion simulation. The ability to
394 estimate the source location with accuracy surpassing the grid size can be attributed to the strong fitting capability of the
395 optimized XGBoost model (Chen and Guestrin, 2016; Grinsztajn et al., 2022). However, this capability, although inherent, is
396 not present across all optimized XGBoost models, as external factors such as observation noises and meteorological data
397 inaccuracies can also impact the accuracy of source location estimation.

398 For the ETEX-1 experiment, the pre-screening zone also covers the true source location for Group 1 and Group 2. The
399 source locations estimated by the correlation-based method are 411.85 km and 486.41 km away from the ground truth for
400 Group 1 and Group 2, respectively. The location error of the Bayesian method estimates is only 30.50 km for Group 1, but
401 increases to 520.77 km for Group 2, indicating the sensitivity of this method to the observations. In contrast, the proposed
402 method achieves much lower source location errors of 5.19 km for Group 1 (a relative error of 0.20%) and 17.65 km for Group
403 2 (a relative error of 0.70%). Group1 exhibits a lower source location error than Group 2, because the observation sites of
404 Group 1 are closer to the sampled source locations than those of Group 2 and better characterize the plume. Feature selection
405 did not remove many features (Fig. 4c and 4d), so the estimated source locations with and without feature selection basically
406 overlap for both groups.



407

408

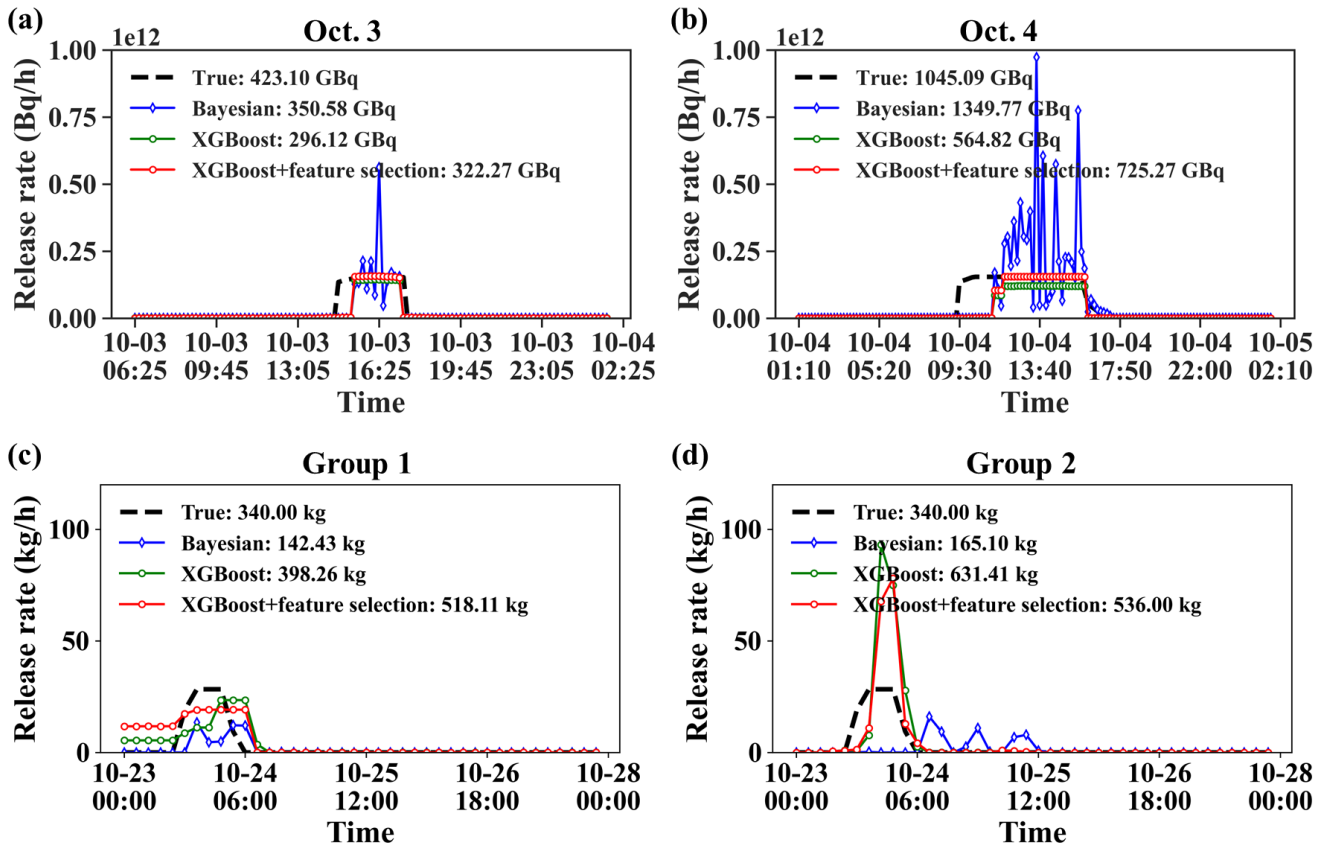
Figure 5. Source location estimation results of SCK-CEN ^{41}Ar experiment: (a) Oct. 3; (b) Oct. 4; and ETEX-1 experiment: (c) Group 1; (d)

409 Group 2. A detailed enlargement of the region around (2.5°W, 47.5°N) to (1.5°W, 48.5°N) is shown in the bottom right corner in (c) and (d)
410 to highlight the source location estimation results of the proposed method. The yellow dots denote the maximum correlation points, which
411 are the results of the correlation-based method. The green and red stars represent the results based on XGBoost before and after feature
412 selection, respectively. The cyan diamonds represent the results based on the Bayesian method.

413 **3.3.2 Release rates**

414 Figure 6 displays the release rates estimated by the Bayesian and PAMILT methods based on the source location estimates in
415 Fig. 5. For the SCK-CEN ⁴¹Ar experiment (Fig. 6a and 6b), the release rates provided by the Bayesian method present several
416 sharp peaks, corresponding to overestimates of up to 269.03% (Oct. 3) and 532.35% (Oct. 4). Furthermore, the Bayesian
417 estimates exhibit unrealistic oscillations in the stable release phase. In contrast, the PAMILT method successfully retrieves the
418 peak releases without oscillations for both days. Both the Bayesian and PAMILT estimates give delayed release start times,
419 but accurately estimate the end times, especially for Oct. 3. The PAMILT estimate underestimates the total release by 30.01%
420 and 45.95% for Oct. 3 and Oct. 4, respectively; these values decrease to about 23.83% and 30.60%, respectively, after feature
421 selection. The Bayesian method gives better total releases because of the overestimated peaks.

422 For the ETEX-1 experiment (Fig. 6c and 6d), the Bayesian estimates exhibit notable fluctuations, leading to
423 underestimations of 58.11% for Group 1 and 51.44% for Group 2. Furthermore, the temporal profile of the Bayesian estimates
424 for Group 2 falls completely outside the true release window. In contrast, most releases using the PAMILT estimates are within
425 the true release time window, especially for Group 2, despite the overestimations reaching 52.38% for Group 1 and 57.65%
426 for Group 2, after the feature selection process. Compared with the SCK-CEN ⁴¹Ar experiment, the increased deviation in the
427 ETEX-1 experiment is caused by the sparsity of observations at the four sites (Fig. S3).



428

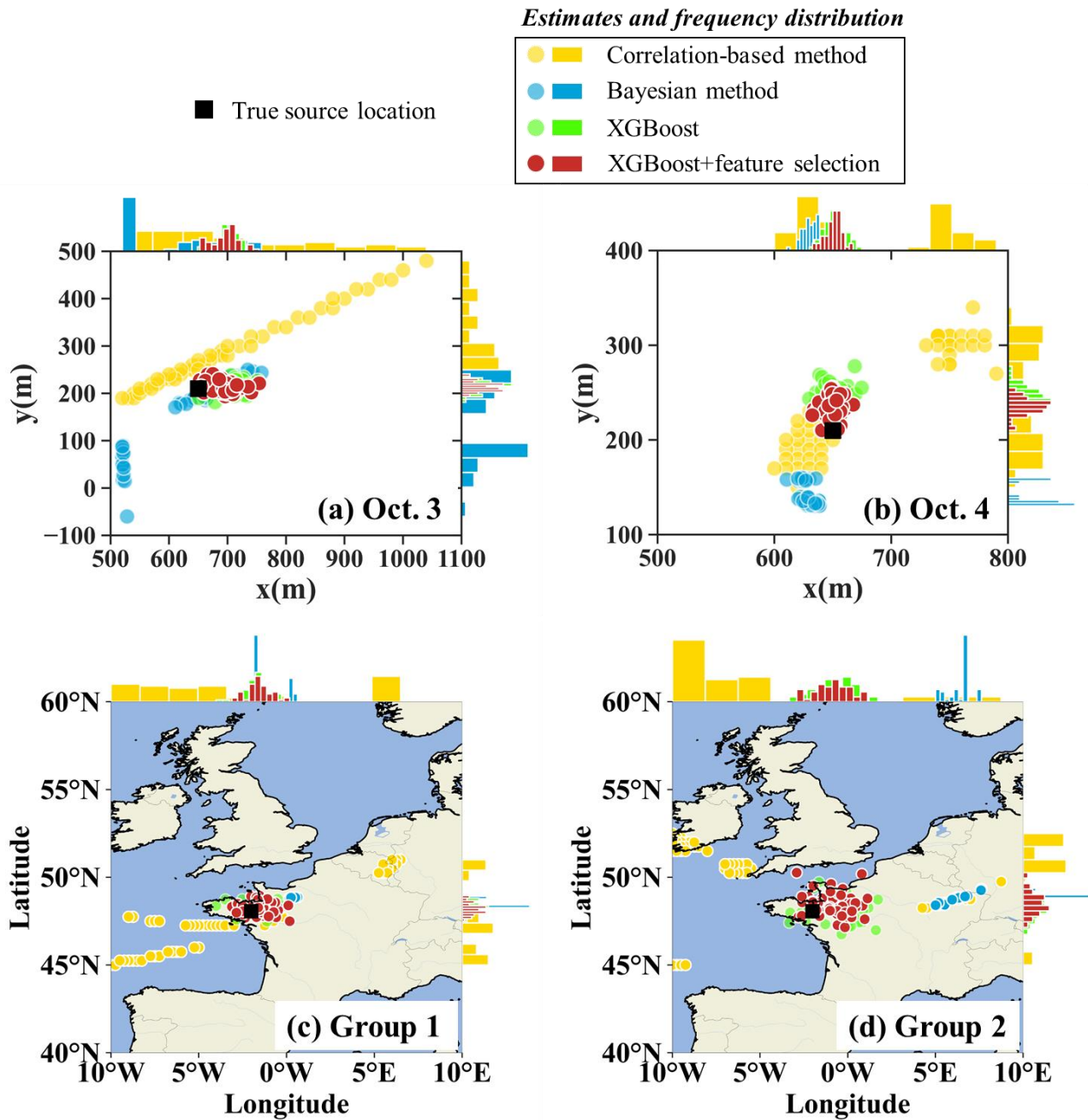
429 **Figure 6.** Release rate estimation results with different location estimates of SCK-CEN ^{41}Ar experiment: (a) Oct. 3; (b) Oct. 4; and ETEX-
 430 1 experiment: (c) Group 1; (d) Group 2. The release rates labelled XGBoost or XGBoost+feature selection are estimated using the PAMILT
 431 method.

432 3.3.3 Uncertainty range

433 Figure 7 compares the spatial distribution of 50 estimates produced by different methods. For the SCK-CEN ^{41}Ar experiment,
 434 the estimates of the correlation-based method are highly dispersed for both days, leading to a very uniform distribution of the
 435 x coordinate for Oct. 3 and two separate distributions of both the coordinates for Oct. 4. The Bayesian method produces a
 436 multimodal distribution for both days, in which the estimates are more concentrated than those of the correlation-based method.
 437 The corresponding full posteriori distributions in Fig. S5(a) and S5(b) better reveal the multimodal feature of the Bayesian
 438 method, with several peaks of similar probabilities in the estimates of both coordinates on Oct. 3 and the y coordinate on Oct.
 439 4. The multimodal feature indicates the difficulty of constraining the solution in simultaneous spatiotemporal reconstruction,
 440 as reported in a previous study (Meutter and Hoffman, 2020). In comparison, the proposed method provides the most
 441 concentrated source location estimates. The feature selection moves the centre of the distribution closer to the true location
 442 and narrows the distribution of the estimates, especially for Oct. 4.

443 For the ETEX-1 experiment, the estimates of the correlation-based method are quite dispersed, whereas those of the

444 Bayesian method are more concentrated. The Bayesian estimates are close to the truth for Group 1, but deviate noticeably for
445 Group 2. This phenomenon indicates that the Bayesian method is sensitive to the observations, especially when the
446 observations are sparse. Figure S5(c) and S5(d) reveals that the Bayesian-estimated posterior distribution is multimodal for
447 both ETEX-1 groups; this can be avoided by using additional observations (Fig. S5e). In contrast, the proposed method
448 provides estimates that are concentrated around the truth for both Group 1 and Group 2, indicating its efficiency in the case of
449 sparse observations. Due to the shorter distance between observation sites and the sampled source locations, the uncertainty
450 range of source location for Group 1 is narrower than that for Group 2.

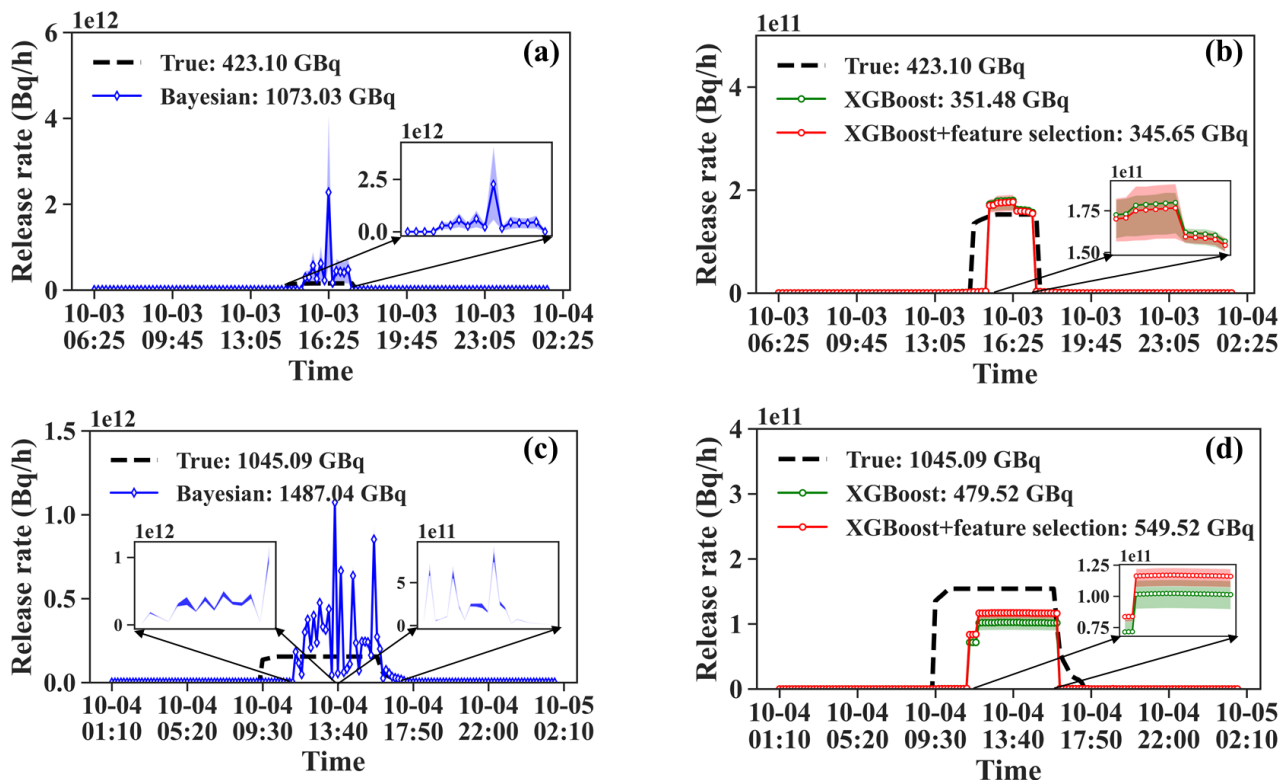


451

452 **Figure 7.** Spatial distribution of 50 source location estimates of SCK-CEN ^{41}Ar experiment: (a) Oct. 3; (b) Oct. 4; and ETEX-1 experiment:
 453 (c) Group 1; (d) Group 2. Each circle denotes an individual estimate as detailed in Sect. 2.8.5, with colour variations indicating the respective
 454 method employed. Histograms along the axes represent the frequency distribution of the estimates along the respective axis.

455 Figure 8 compares the uncertainty range and mean total release of the release rate estimations for the SCK-CEN ^{41}Ar
 456 experiment. For Oct. 3, the Bayesian estimates significantly overestimate the mean values and have a large uncertainty range,

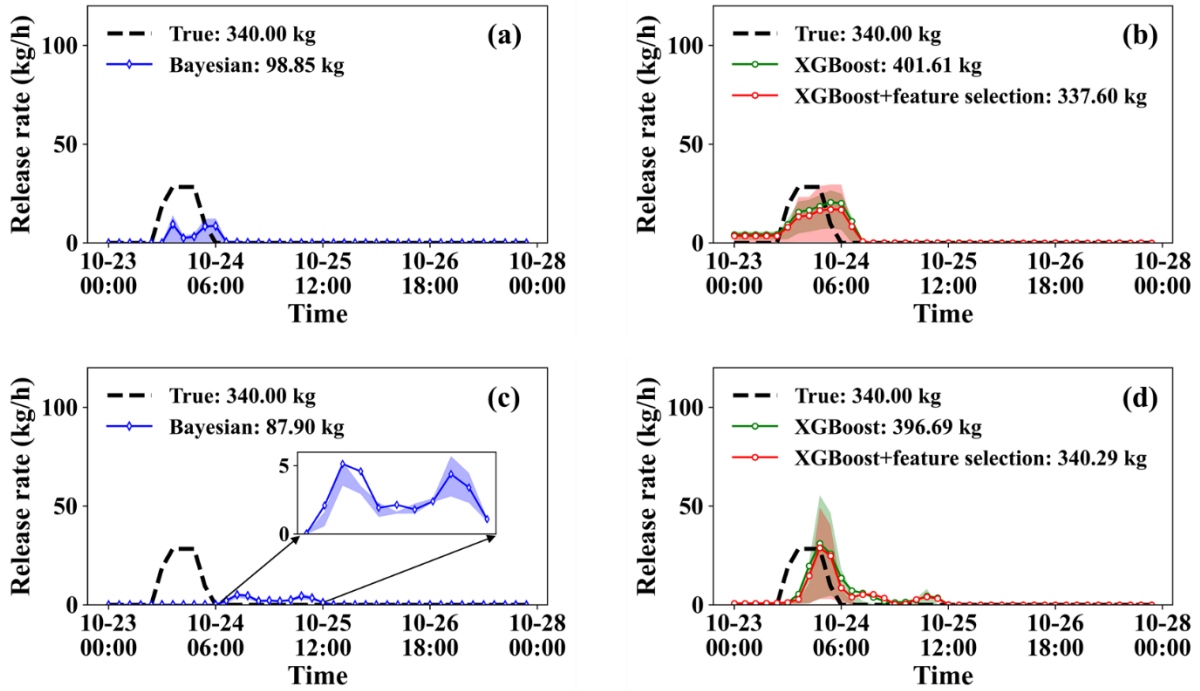
457 whereas the mean PAMILT estimate is very close to the true release and the uncertainty range is smaller than that of the
 458 Bayesian method. For Oct. 4, the mean Bayesian estimate exhibits greater deviations than the mean PAMILT estimate. Feature
 459 selection improves the mean estimate and reduces the uncertainty range of PAMILT because it improves the source location
 460 estimation, thus reducing the deviation in the inverse model of the release rate. On Oct. 3 and Oct. 4, the PAMILT method
 461 underestimates the total release by 18.30% and 47.42%, respectively, whereas the Bayesian method gives overestimations of
 462 153.61% and 42.29%, respectively.



463
 464 **Figure 8.** Release rate estimates over 50 calculations of SCK-CEN ^{41}Ar experiment. (a) Oct. 3-Bayesian method; (b) Oct. 3-PAMILT method;
 465 (c) Oct. 4-Bayesian method; (d) Oct. 4-PAMILT method. The shadow represents the uncertainty range between the lower quartile and the
 466 upper quartile. The shadow of each figure is amplified by an enlarged subgraph. The legends in each figure provide the mean estimates for
 467 the total release.

468 Figure 9 compares the uncertainty ranges of the release rate estimates for the two ETEX-1 groups. For both groups, the
 469 Bayesian estimates exhibit noticeable underestimations (including the mean estimate) and small uncertainty ranges (Fig. 9a
 470 and 9c). The Bayesian estimates fall completely outside the true release window for Group 2 (Fig. 9c). The mean PAMILT
 471 estimates are more accurate than the mean Bayesian estimates, with most releases within the true release window (Fig. 9b and
 472 9d). However, the PAMILT estimates have a large uncertainty range for the ETEX-1 experiment than for the SCK-CEN ^{41}Ar
 473 experiment, implying that the source–receptor matrices of the ETEX-1 experiment are more sensitive to errors in source
 474 location than those of the SCK-CEN ^{41}Ar experiment. This greater sensitivity originates from the complex meteorology in the

475 ETEX-1 experiment. As for the mean total releases, the Bayesian method produces underestimations of 70.93% for Group1
 476 and 74.15% for Group2. In comparison, the proposed method gives deviations of only 0.71% for Group 1 and 0.09% for Group
 477 2, after feature selection.



478

479 **Figure 9.** Release rate estimates over 50 calculations of ETEX-1 experiment. (a) Group 1-Bayesian method; (b) Group 1-PAMILT method;
 480 (c) Group 2-Bayesian method; (d) Group 2-PAMILT method.

481 Table 4 lists the mean and standard deviation of the relative errors for the 50 estimates given by different methods. The
 482 correlation-based method produces the largest mean relative error and standard deviation for source location estimation, except
 483 for Group 2 of ETEX-I. For the SCK-CEN ⁴¹Ar experiment, the proposed method gives the smallest mean error, about half of
 484 that of the Bayesian method. Its standard deviation is around one-quarter of that of the Bayesian method for Oct. 3, but is
 485 slightly larger for Oct. 4. For the total release, the PAMILT method gives a better standard deviation of the relative error for
 486 both days and a better mean relative error for Oct. 3, whereas the Bayesian method produces a better mean relative error for
 487 Oct. 4. Feature selection reduces the mean relative error, except for the total release for Oct. 3, and slightly increases the
 488 standard deviation of the source location and total release results for Oct. 3. The mean relative error of the total release averaged
 489 on the two days is 65.09% lower than that of the Bayesian method.

490 For the ETEX-1 experiment, the Bayesian method exhibits case-sensitive performances with respect to the mean relative
 491 error of source location estimation, whereas the proposed method gives the most accurate source locations with small
 492 uncertainties for both groups. As for the total release, the proposed method gives smaller mean relative errors than the Bayesian
 493 methods, but the Bayesian method has a smaller standard deviation. Feature selection significantly reduces the mean relative

494 error for the two groups. The mean relative error of the total release averaged over the two groups is 72.14% lower than that
 495 of the Bayesian method.

496 **Table 4.** Relative errors of source reconstruction. δ_r represents the relative error of source location, which is positive and δ_Q denotes the
 497 relative error of total release, where a positive value indicates overestimation and a negative value denotes underestimation.

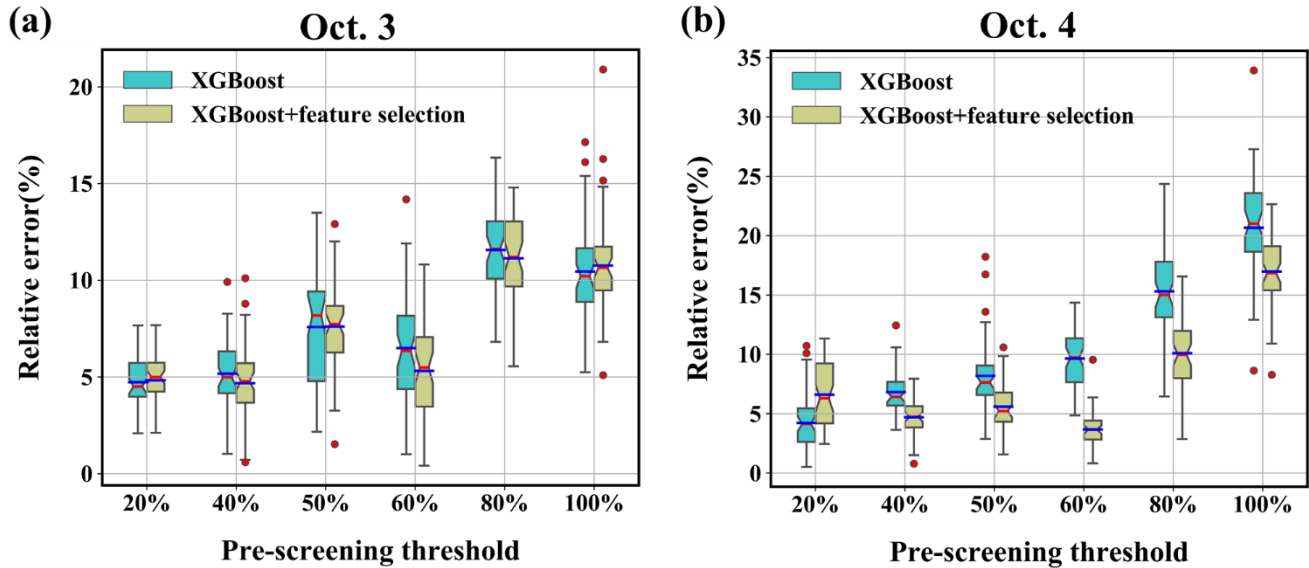
Experiment	Case	Statistical parameters (Relative error)	Correlation-based method	Bayesian method	The proposed method			
					XGBoost	XGBoost+ feature selection		
SCK-CEN ⁴¹ Ar	Oct. 3	δ_r	Mean	14.10%	11.88%	5.18%	4.68%	
			Std	11.37%	7.53%	1.79%	2.05%	
		δ_Q	Mean	-	153.61%	-16.93%	-18.30%	
			Std	-	189.76%	9.45%	8.01%	
		Oct. 4	δ_r	Mean	14.30%	12.83%	6.83%	4.71%
				Std	9.60%	1.68%	1.76%	1.53%
	δ_Q		Mean	-	42.29%	-54.12%	-47.42%	
			Std	-	15.05%	6.47%	5.85%	
	ETEX-I	Group 1	δ_r	Mean	16.95%	3.22%	2.32%	2.42%
				Std	7.46%	2.75%	1.43%	1.43%
			δ_Q	Mean	-	-70.93%	18.12%	-0.71%
				Std	-	17.87%	99.85%	102.01%
Group 2			δ_r	Mean	21.9%	23.97%	5.21%	4.97%
				Std	5.05%	1.97%	2.42%	2.35%
		δ_Q	Mean	-	-74.15%	16.67%	0.09%	
			Std	-	11.68%	93.50%	109.56%	

498 **3.4 Sensitivity analysis results**

499 **3.4.1 Sensitivity to the search range**

500 Figure 10 displays the source location errors obtained using different pre-screening thresholds to determine the search range.
 501 The error is smaller with a lower threshold, implying that a small search range helps reduce the mean and median errors. As
 502 the threshold increases, the mean and median errors, as well as the error range, show an overall tendency to increase, but not

503 in a strictly monotonic way. The mean/median error is less than 12% for Oct. 3 and less than 22% for Oct. 4, indicating robust
 504 performance in these tests. Feature selection reduces the mean/median, range, and the lower bound of the errors in most tests,
 505 demonstrating its efficiency.

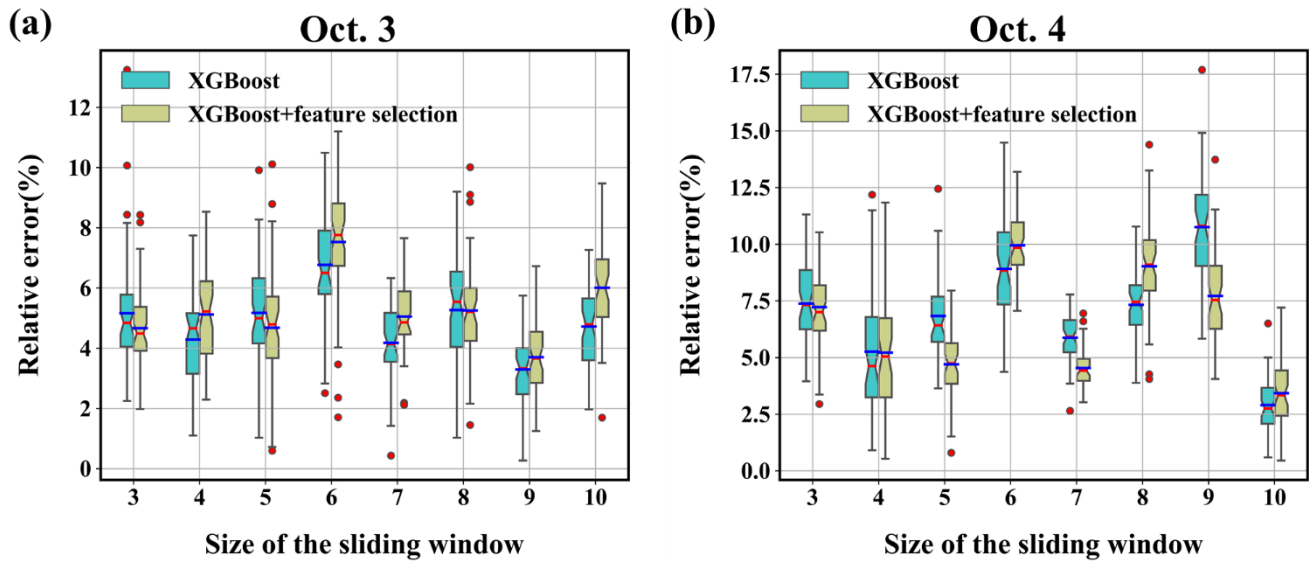


506

507 **Figure 10.** Distribution of relative error (%) over 50 runs with different search ranges. The blue and red solid lines denote average relative
 508 error (%) and median relative error (%), respectively. The upper and lower boundaries represent the upper and lower quartiles of relative
 509 error (%), respectively. The fences are 1.5 times the inter-quartile ranges of the upper/lower quartiles. The red circles denote data that are
 510 not included between the fences. (a) Oct. 3; (b) Oct. 4.

511 3.4.2 Sensitivity to the size of the sliding window

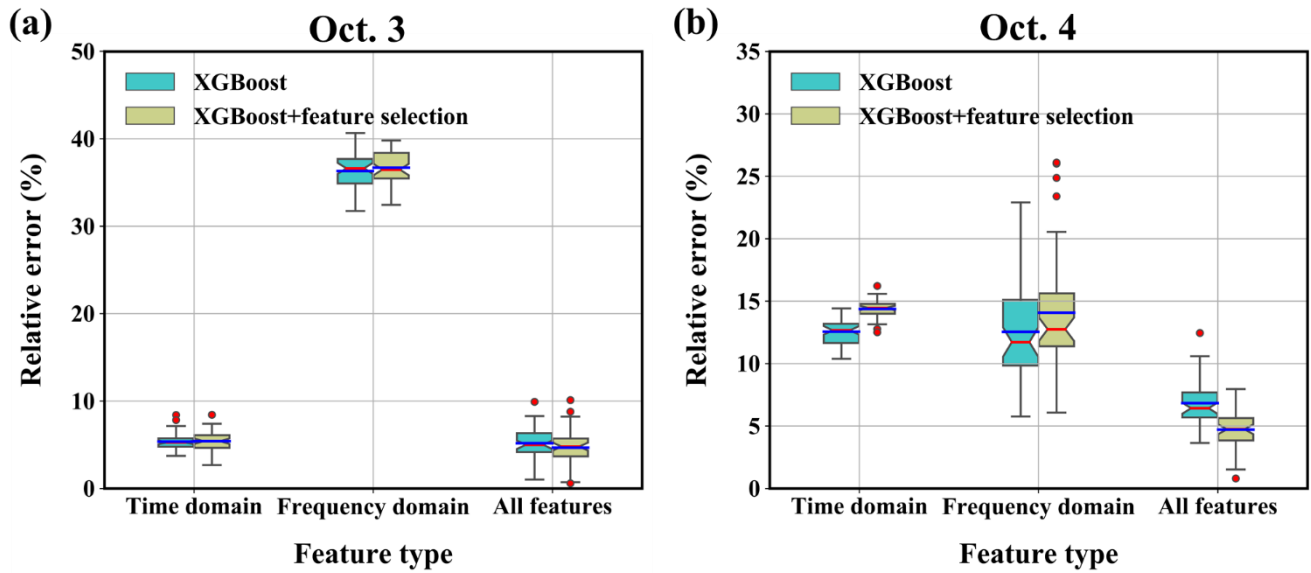
512 Figure 11 shows the source location errors obtained with different sliding-window sizes. The mean/median error is less than
 513 8% for Oct. 3 and less than 11% for Oct. 4, both of which are smaller than for the various search ranges. This indicates that
 514 the proposed method is more robust to this parameter than to the search range. For both days, the lowest mean/median and
 515 error range occur with relatively large window sizes, i.e. window size of 9 for Oct. 3 and window size of 10 for Oct. 4. This is
 516 because a large window size increases the strength of the filtering and removes the temporal variations in the release rates
 517 more completely. However, a large window size leads to increased computational cost. Because the errors vary in a limited
 518 range, a medium window size provides a better balance between accuracy and computational cost. Feature selection improves
 519 the results for medium and small window sizes, but may have less effect with large window sizes. This tendency implies that
 520 it is more appropriate to apply feature selection with medium window sizes than with large window sizes, as in this study.



521
522 **Figure 11.** Sensitivity to the size of the sliding window. (a) Oct. 3; (b) Oct. 4.

523 **3.4.3 Sensitivity to the feature type**

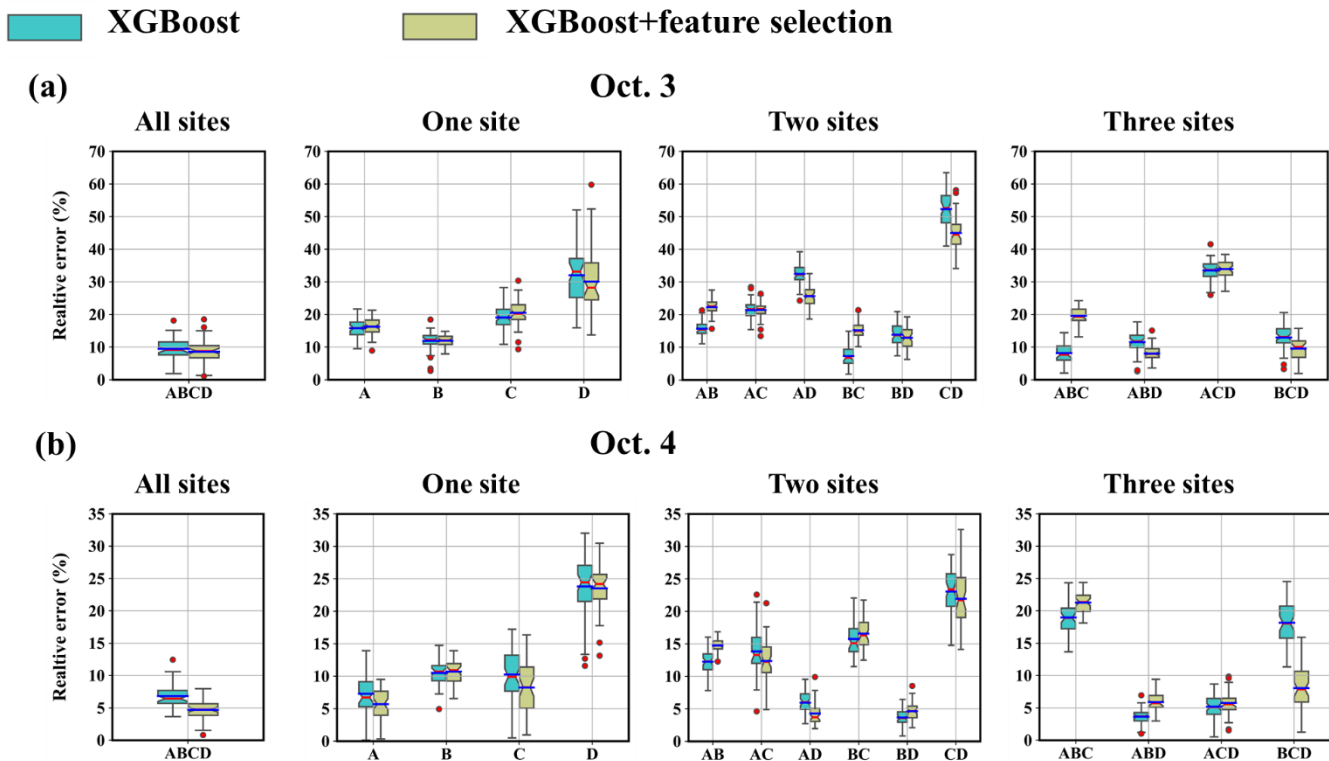
524 Figure 12 compares the results obtained with different feature types. For Oct. 3, the source location errors are quite low when
525 using only the time-domain features for the reconstruction; indeed, the errors are only slightly larger than when using all the
526 features. In contrast, the results obtained using only the frequency-domain features exhibit larger errors, indicating that the
527 time-domain features make a greater contribution to the results for Oct. 3. For Oct. 4, the mean source location errors are
528 similar when using either the time- or frequency-domain features, but the error range is higher when the frequency-domain
529 features are used. In addition, the errors of both single-domain-feature results are higher than those of the all-feature results,
530 indicating that both feature types should be included to ensure accurate and robust source location estimation.



531
532 **Figure 12.** Sensitivity to the feature type. (a) Oct. 3; (b) Oct. 4.

533 **3.4.4 Sensitivity to the number and combination of observation sites**

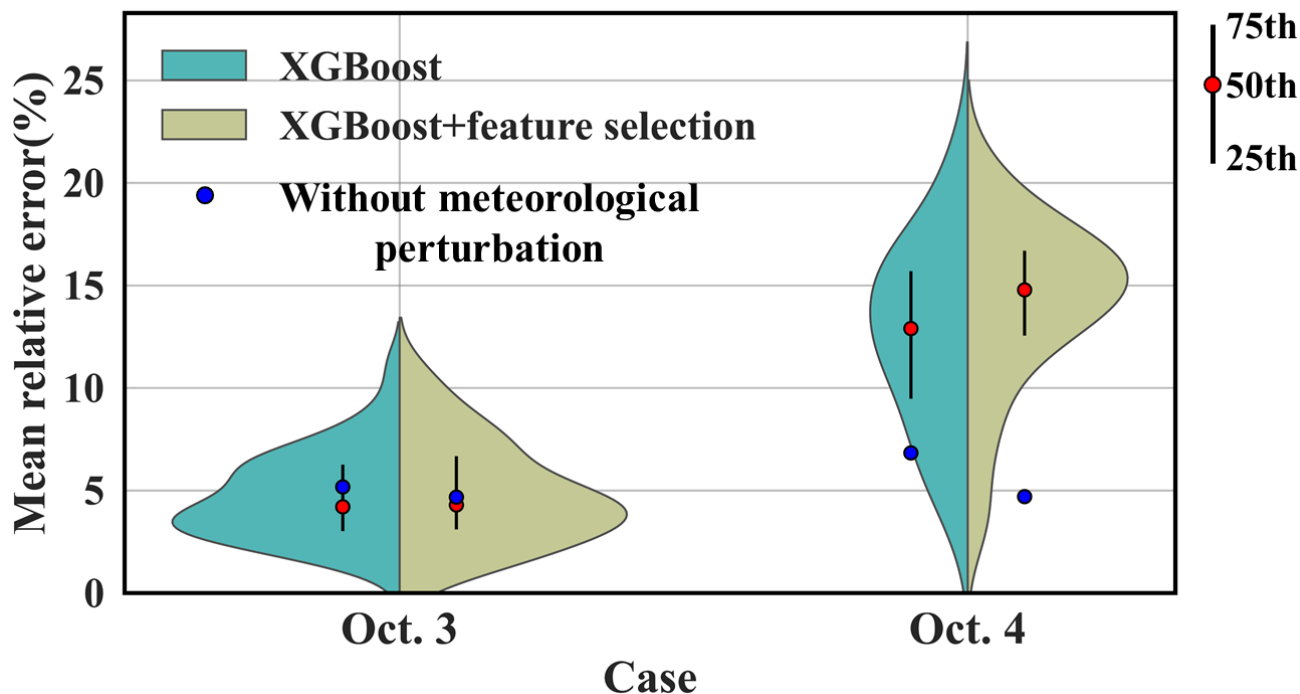
534 Figure 13 compares the results obtained with different numbers and combinations of observation sites. The results indicate
 535 that the source location error may be more sensitive to the position of the observation site than to the number of sites included.
 536 The error level of all-site estimations is relatively low for both days, indicating that increasing the number of observation sites
 537 better constrains the solution and help improve the robustness of the model. However, the lowest error levels are achieved by
 538 a subset of sites, i.e. Site ABD on Oct. 3 and Site BD on Oct. 4. This is possibly because including all observation sites may
 539 cause overfitting and reduce the prediction accuracy. This overfitting can be alleviated by using only representative sites at
 540 appropriate position, which capture the environmental variability and provide clear information for locating the source. For
 541 Oct.3, multi-site estimations with Site B always produce low error levels, and single-site estimation using Site B also achieves
 542 high accuracy. For Oct.4, multi-site estimations with Site BD always achieve relatively low error levels. These results
 543 demonstrate the importance of using representative sites for source location estimation. The representative sites (Site B for
 544 Oct. 3 and Site BD for Oct. 4) are consistent with the importance calculated in the feature selection step (Fig. 4), preliminarily
 545 indicating the potential for feature selection to identify representative sites. In addition, feature selection reduces the mean
 546 error level in most cases.



547
548 **Figure 13.** Sensitivity to the number and combination of observation sites. (a) Oct. 3; (b) Oct. 4.

549 **3.4.5 Sensitivity to the meteorological errors**

550 Figure 14 illustrates the distribution of mean relative source location errors (averaged across 50 groups of hyperparameters)
 551 retrieved with 50 perturbed meteorological inputs. For Oct. 3, the estimates generally present a low error level (generally below
 552 10%), and the 50th error level is lower than the error of the unperturbed results (4.68%). In comparison, for Oct. 4, most
 553 perturbed results exhibit larger errors (primarily 10%–20%) than the unperturbed result (4.71%), indicating that models for
 554 Oct. 4 are more sensitive to the meteorological errors. This sensitivity difference results from the layout of the observation
 555 sites (Fig. 2a). The sites on Oct. 3 were almost perpendicular to the prevailing wind direction, capturing the plume under a
 556 large range of wind directions. In contrast, the sites on Oct. 4 were basically parallel to the wind direction, capturing the plume
 557 only for a very limited range of wind directions. This result indicates the importance of site layout for robust reconstruction in
 558 the presence of meteorological errors. Feature selection slightly changes the mean relative error distribution and its percentiles
 559 for both days, indicating that meteorological errors may alter the importance of each feature and reduce the effectiveness of
 560 feature selection. In addition to meteorological errors, dispersion errors such as wet deposition parameterization (Zhuang et
 561 al., 2023) may influence the result, but these errors are not dominant in the two field experiments. The handling of such
 562 dispersion errors will be investigated in future work.



563

564 **Figure 14.** Sensitivity to the meteorological errors. The violin plots illustrate the kernel density estimation of errors under different
 565 meteorological groups for XGBoost models before and after feature selection. The vertical black lines inside the violins depict the
 566 interquartile range, capturing the 25th, 50th (red dots), and 75th percentiles of mean relative errors. The blue dots denote the mean relative
 567 source location errors for models without meteorological perturbation, as listed in Table 4.

568 4. Conclusions

569 In this study, we relaxed the unrealistic constant-release assumption of source reconstruction. Instead, we took advantage of
 570 the fact that most atmospheric radionuclide releases have a spatially fixed source, and thus the release rate mainly influences
 571 the peak values in the temporal observations. Based on this, a more general spatiotemporally separated source reconstruction
 572 method was developed to estimate non-constant releases. The separation process was achieved by applying a temporal sliding-
 573 window average filter to the observations. This filter reduces the influence of temporal variations in the release rates on the
 574 observations, so that the relative spatiotemporal distribution of the filtered observations is dominated by the source location
 575 and known meteorology. A response feature vector was extracted to quantify the long-term temporal response trends at each
 576 observation site, involving tailored indicators of both the time and frequency domains. The XGBoost algorithm was used to
 577 train a machine learning model that links the source location to the feature vector, enabling independent source location
 578 estimation without knowing the release rate. With the retrieved source location, the detailed temporal variations of the release
 579 rate were determined using the PAMILT algorithm. Validation was performed against the two-day SCK-CEN ^{41}Ar field
 580 experimental data and two groups of ETEX-1 data. The results demonstrate that the proposed method successfully removes

581 the influence of temporal variations in release rates across observations and accurately reconstructs both the spatial location
582 and temporal variations of the source.

583 For the local-scale SCK-CEN ^{41}Ar experiment, source location was reconstructed with lowest errors of only 0.60% (Oct. 3)
584 and 0.80% (Oct. 4), significantly lower than for the correlation-based method and Bayesian method. In terms of the release
585 rate, the PAMILT method reconstructed the temporal variations, peak, and total release with high accuracy, thus avoiding the
586 unrealistic oscillations given by the Bayesian estimate. The proposed method produced smaller uncertainty ranges than the
587 Bayesian method and avoided the multimodal distribution of the Bayesian method. The feature selection process removed the
588 redundant features and reduced the reconstruction errors. For the continental-scale ETEX-1 experiment, the lowest relative
589 source location errors were 0.20% and 0.70% for Group 1 and Group 2, respectively, which were again lower than for the
590 correlation-based and Bayesian methods. The proposed method provides highly accurate mean estimates of the release rate for
591 both groups, although with a large uncertainty range.

592 Sensitivity analyses on the SCK-CEN ^{41}Ar experiment revealed that the proposed method exhibits stable source location
593 estimation performance with different parameters and remains effective with only a single observation site, as long as the
594 selected site is appropriately located. Moreover, the proposed method shows robust source location estimation in the presence
595 of meteorological errors, with mean source location error levels below 10%, on condition that the site layout is appropriate.

596 These results demonstrate that spatiotemporally separated source reconstruction is feasible and achieves satisfactory
597 accuracy in multi-scale release scenarios, thereby providing a promising framework for reconstructing atmospheric
598 radionuclide releases. However, the proposed method does not consider the influence of temporal variations in the release rate
599 on the plume shape. Our future efforts will be directed towards integrating spatial features to further enhance the method.

600

601 *Code and data availability.* The code and data for the proposed method can be downloaded from Zenodo
602 (<https://doi.org/10.5281/zenodo.10200141>). More recent versions of the code and data will be published on GitHub.com
603 (<https://github.com/rocketlab/Source-reconstruction-of-non-constant-atmospheric-radionuclide-releases>, last access: 23
604 November 2023). The implementation is provided in Python, and the instruction file is also available in the provided link.

605

606 *Author contributions.* YX conducted the source reconstruction tests and wrote the manuscript draft; SF provided guidance on
607 the RIMPUFF modeling and suggestions on source reconstruction tests; XD and SZ reviewed and edited the manuscript.

608

609 *Competing interests.* The authors have declared that they have no conflict of interest.

610

611 *Acknowledgements.* This work is supported by the National Natural Science Foundation of China (grant numbers 12275152
612 and 11875037), LingChuang Research Project of China National Nuclear Corporation, and International Atomic Energy
613 Agency (TC project number CRP9053).

614 **References**

- 615 Akhtar, F., Li, J., Pei, Y., Xu, Y., Rajput, A., and Wang, Q.: Optimal Features Subset Selection for Large for Gestational
616 Age Classification Using GridSearch Based Recursive Feature Elimination with Cross-Validation Scheme, in: International
617 Conference on Frontier Computing, 63–71, https://doi.org/10.1007/978-981-15-3250-4_8, 2019.
- 618 Andronopoulos, S. and Kovalets, I. V.: Method of source identification following an accidental release at an unknown
619 location using a lagrangian atmospheric dispersion model, *Atmosphere (Basel)*, 12, 7–12,
620 <https://doi.org/10.3390/atmos12101305>, 2021.
- 621 Anspaugh, L. R., Catlin, R. J., and Goldman, M.: The global impact of the chernobyl reactor accident, *Science (80-.)*, 242,
622 1513–1519, <https://doi.org/10.1126/science.3201240>, 1988.
- 623 Becker, A., Wotawa, G., De Geer, L. E., Seibert, P., Draxler, R. R., Sloan, C., D'Amours, R., Hort, M., Glaab, H., Heinrich,
624 P., Grillon, Y., Shershakov, V., Katayama, K., Zhang, Y., Stewart, P., Hirtl, M., Jean, M., and Chen, P.: Global backtracking
625 of anthropogenic radionuclides by means of a receptor oriented ensemble dispersion modelling system in support of Nuclear-
626 Test-Ban Treaty verification, *Atmos. Environ.*, 41, 4520–4534, <https://doi.org/10.1016/j.atmosenv.2006.12.048>, 2007.
- 627 Chang, J. C. and Hanna, S. R.: Air quality model performance evaluation, *Meteorol. Atmos. Phys.*, 87, 167–196,
628 <https://doi.org/10.1007/s00703-003-0070-7>, 2004.
- 629 Chen, T. and Guestrin, C.: XGBoost: A scalable tree boosting system, *Proc. ACM SIGKDD Int. Conf. Knowl. Discov. Data*
630 *Min.*, 13-17-Aug, 785–794, <https://doi.org/10.1145/2939672.2939785>, 2016.
- 631 Chow, F. K., Kosović, B., and Chan, S.: Source inversion for contaminant plume dispersion in urban environments using
632 building-resolving simulations, *J. Appl. Meteorol. Climatol.*, 47, 1533–1572, <https://doi.org/10.1175/2007JAMC1733.1>,
633 2008.
- 634 Davoine, X. and Bocquet, M.: Inverse modelling-based reconstruction of the Chernobyl source term available for long-range
635 transport, *Atmos. Chem. Phys.*, 7, 1549–1564, <https://doi.org/10.5194/acp-7-1549-2007>, 2007.
- 636 Drews, M., Aage, H. K., Bargholz, K., Ejsing Jørgensen, H., Korsbech, U., Lauritzen, B., Mikkelsen, T., Rojas-Palma, C.,
637 and Ammel, R. Van: Measurements of plume geometry and argon-41 radiation field at the BR1 reactor in Mol, Belgium, 1–
638 43 pp., 2002.
- 639 Dumont Le Brazidec, J., Bocquet, M., Saunier, O., and Roustan, Y.: MCMC methods applied to the reconstruction of the
640 autumn 2017 Ruthenium-106 atmospheric contamination source, *Atmos. Environ. X*, 6, 100071,
641 <https://doi.org/10.1016/j.aeaoa.2020.100071>, 2020.
- 642 Dumont Le Brazidec, J., Bocquet, M., Saunier, O., and Roustan, Y.: Quantification of uncertainties in the assessment of an
643 atmospheric release source applied to the autumn 2017 106Ru event, *Atmos. Chem. Phys.*, 21, 13247–13267,
644 <https://doi.org/10.5194/acp-21-13247-2021>, 2021.
- 645 Eamonn Keogh, Selina Chu, D. H. and M. P.: SEGMENTING TIME SERIES: A SURVEY AND NOVEL APPROACH, in:
646 *Data mining in time series databases*, 1–21, https://doi.org/10.1142/9789812565402_0001, 2004.

647 Efthimiou, G. C., Kovalets, I. V., Venetsanos, A., Andronopoulos, S., Argyropoulos, C. D., and Kakosimos, K.: An
648 optimized inverse modelling method for determining the location and strength of a point source releasing airborne material
649 in urban environment, *Atmos. Environ.*, 170, 118–129, <https://doi.org/10.1016/j.atmosenv.2017.09.034>, 2017.

650 Efthimiou, G. C., Kovalets, I. V., Argyropoulos, C. D., Venetsanos, A., Andronopoulos, S., and Kakosimos, K. E.:
651 Evaluation of an inverse modelling methodology for the prediction of a stationary point pollutant source in complex urban
652 environments, *Build. Environ.*, 143, 107–119, <https://doi.org/10.1016/j.buildenv.2018.07.003>, 2018.

653 Eslinger, P. W. and Schrom, B. T.: Multi-detection events, probability density functions, and reduced location area, *J.*
654 *Radioanal. Nucl. Chem.*, 307, 1599–1605, <https://doi.org/10.1007/s10967-015-4339-3>, 2016.

655 Fang, S., Dong, X., Zhuang, S., Tian, Z., Chai, T., Xu, Y., Zhao, Y., Sheng, L., Ye, X., and Xiong, W.: Oscillation-free
656 source term inversion of atmospheric radionuclide releases with joint model bias corrections and non-smooth competing
657 priors, *J. Hazard. Mater.*, 440, <https://doi.org/10.1016/j.jhazmat.2022.129806>, 2022.

658 Grinsztajn, L., Oyallon, E., and Varoquaux, G.: Why do tree-based models still outperform deep learning on tabular data?,
659 2022.

660 Guo, S., Yang, R., Zhang, H., Weng, W., and Fan, W.: Source identification for unsteady atmospheric dispersion of
661 hazardous materials using Markov Chain Monte Carlo method, *Int. J. Heat Mass Transf.*, 52, 3955–3962,
662 <https://doi.org/10.1016/j.ijheatmasstransfer.2009.03.028>, 2009.

663 Ingremeau, J. and Saunier, O.: Investigations on the source term of the detection of radionuclides in North of Europe in June
664 2020, *EPJ Nucl. Sci. Technol.*, 8, 10, <https://doi.org/10.1051/epjn/2022003>, 2022.

665 Jensen, D. D., Lucas, D. D., Lundquist, K. A., and Glascoe, L. G.: Sensitivity of a Bayesian source-term estimation model to
666 spatiotemporal sensor resolution, *Atmos. Environ. X*, 3, <https://doi.org/10.1016/j.aeaoa.2019.100045>, 2019.

667 Katata, G., Ota, M., Terada, H., Chino, M., and Nagai, H.: Atmospheric discharge and dispersion of radionuclides during the
668 Fukushima Dai-ichi Nuclear Power Plant accident. Part I: Source term estimation and local-scale atmospheric dispersion in
669 early phase of the accident, *J. Environ. Radioact.*, 109, 103–113, <https://doi.org/10.1016/j.jenvrad.2012.02.006>, 2012.

670 Keats, A., Yee, E., and Lien, F. S.: Bayesian inference for source determination with applications to a complex urban
671 environment, *Atmos. Environ.*, 41, 465–479, <https://doi.org/10.1016/j.atmosenv.2006.08.044>, 2007.

672 Keats, A., Yee, E., and Lien, F. S.: Information-driven receptor placement for contaminant source determination, *Environ.*
673 *Model. Softw.*, 25, 1000–1013, <https://doi.org/10.1016/j.envsoft.2010.01.006>, 2010.

674 KIM, J. Y., JANG, H.-K., and LEE, J. K.: Source Reconstruction of Unknown Model Parameters in Atmospheric Dispersion
675 Using Dynamic Bayesian Inference, *Prog. Nucl. Sci. Technol.*, 1, 460–463, <https://doi.org/10.15669/pnst.1.460>, 2011.

676 Kovalets, I. V., Efthimiou, G. C., Andronopoulos, S., Venetsanos, A. G., Argyropoulos, C. D., and Kakosimos, K. E.:
677 Inverse identification of unknown finite-duration air pollutant release from a point source in urban environment, *Atmos.*
678 *Environ.*, 181, 82–96, <https://doi.org/10.1016/j.atmosenv.2018.03.028>, 2018.

679 Kovalets, I. V., Romanenko, O., and Synkevych, R.: Adaptation of the RODOS system for analysis of possible sources of
680 Ru-106 detected in 2017, *J. Environ. Radioact.*, 220–221, <https://doi.org/10.1016/j.jenvrad.2020.106302>, 2020.

681 Li, X., Xiong, W., Hu, X., Sun, S., Li, H., Yang, X., Zhang, Q., Nibart, M., Albergel, A., and Fang, S.: An accurate and
682 ultrafast method for estimating three-dimensional radiological dose rate fields from arbitrary atmospheric radionuclide
683 distributions, *Atmos. Environ.*, 199, 143–154, <https://doi.org/10.1016/j.atmosenv.2018.11.001>, 2019a.

684 Li, X., Sun, S., Hu, X., Huang, H., Li, H., Morino, Y., Wang, S., Yang, X., Shi, J., and Fang, S.: Source inversion of both
685 long- and short-lived radionuclide releases from the Fukushima Daiichi nuclear accident using on-site gamma dose rates, *J.*
686 *Hazard. Mater.*, 379, 120770, <https://doi.org/10.1016/j.jhazmat.2019.120770>, 2019b.

687 Lucas, D. D., Simpson, M., Cameron-Smith, P., and Baskett, R. L.: Bayesian inverse modeling of the atmospheric transport
688 and emissions of a controlled tracer release from a nuclear power plant, *Atmos. Chem. Phys.*, 17, 13521–13543,
689 <https://doi.org/10.5194/acp-17-13521-2017>, 2017.

690 Ma, D., Tan, W., Wang, Q., Zhang, Z., Gao, J., Wang, X., and Xia, F.: Location of contaminant emission source in
691 atmosphere based on optimal correlated matching of concentration distribution, *Process Saf. Environ. Prot.*, 117, 498–510,
692 <https://doi.org/10.1016/j.psep.2018.05.028>, 2018.

693 Masson, O., Steinhauser, G., Zok, D., Saunier, O., Angelov, H., Babić, D., Bečková, V., Bieringer, J., Bruggeman, M.,
694 Burbidge, C. I., Conil, S., Dalheimer, A., De Geer, L. E., De Vismes Ott, A., Eleftheriadis, K., Estier, S., Fischer, H.,
695 Garavaglia, M. G., Gasco Leonarte, C., Gorzkiewicz, K., Hainz, D., Hoffman, I., Hýža, M., Isajenko, K., Karhunen, T.,
696 Kastlander, J., Katzlberger, C., Kierepko, R., Knetsch, G. J., Kövendiné Kónyi, J., Lecomte, M., Mietelski, J. W., Min, P.,
697 Møller, B., Nielsen, S. P., Nikolic, J., Nikolovska, L., Penev, I., Petrinc, B., Povinec, P. P., Querfeld, R., Raimondi, O.,
698 Ransby, D., Ringer, W., Romanenko, O., Rusconi, R., Saey, P. R. J., Samsonov, V., Šilobritiene, B., Simion, E., Söderström,
699 C., Šoštarić, M., Steinkopff, T., Steinmann, P., Sýkora, I., Tabachnyi, L., Todorovic, D., Tomankiewicz, E., Tschiersch, J.,
700 Tsibranski, R., Tzortzis, M., Ungar, K., Vidic, A., Weller, A., Wershofen, H., Zagyvai, P., Zalewska, T., Zapata García, D.,
701 and Zorko, B.: Airborne concentrations and chemical considerations of radioactive ruthenium from an undeclared major
702 nuclear release in 2017, *Proc. Natl. Acad. Sci. U. S. A.*, 116, 16750–16759, <https://doi.org/10.1073/pnas.1907571116>, 2019.

703 Mekhaimr, S. A. and Abdel Wahab, M. M.: Sources of uncertainty in atmospheric dispersion modeling in support of
704 Comprehensive Nuclear–Test–Ban Treaty monitoring and verification system, *Atmos. Pollut. Res.*, 10, 1383–1395,
705 <https://doi.org/10.1016/j.apr.2019.03.008>, 2019.

706 Meutter, P. De and Hoffman, I.: Bayesian source reconstruction of an anomalous Selenium-75 release at a nuclear research
707 institute, *J. Environ. Radioact.*, 218, 106225, <https://doi.org/10.1016/j.jenvrad.2020.106225>, 2020.

708 De Meutter, P., Hoffman, I., and Ungar, K.: On the model uncertainties in Bayesian source reconstruction using an ensemble
709 of weather predictions, the emission inverse modelling system FREAR v1.0, and the Lagrangian transport and dispersion
710 model Flexpart v9.0.2, *Geosci. Model Dev.*, 14, 1237–1252, <https://doi.org/10.5194/gmd-14-1237-2021>, 2021.

711 Monache, L. D., Lundquist, J. K., Kosoví, B., Johannesson, G., Dyer, K. M., Aines, R. D., Chow, F. K., Belles, R. D.,
712 Hanley, W. G., Larsen, S. C., Loosmore, G. A., Nitao, J. J., Sugiyama, G. A., and Vogt, P. J.: Bayesian inference and
713 Markov Chain Monte Carlo sampling to reconstruct a contaminant source on a continental scale, *J. Appl. Meteorol.*
714 *Climatol.*, 47, 2600–2613, <https://doi.org/10.1175/2008JAMC1766.1>, 2008.

715 Nodop, K., Connolly, R., and Girardi, F.: The field campaigns of the European tracer experiment (ETEX): Overview and
716 results, *Atmos. Environ.*, 32, 4095–4108, [https://doi.org/10.1016/S1352-2310\(98\)00190-3](https://doi.org/10.1016/S1352-2310(98)00190-3), 1998.

717 Pisso, I., Sollum, E., Grythe, H., Kristiansen, N. I., Cassiani, M., Eckhardt, S., Arnold, D., Morton, D., Thompson, R. L.,
718 Groot Zwaaftink, C. D., Evangeliou, N., Sodemann, H., Haimberger, L., Henne, S., Brunner, D., Burkhart, J. F., Fouilloux,
719 A., Brioude, J., Philipp, A., Seibert, P., and Stohl, A.: The Lagrangian particle dispersion model FLEXPART version 10.4,
720 *Geosci. Model Dev.*, 12, 4955–4997, <https://doi.org/10.5194/gmd-12-4955-2019>, 2019.

721 Rajaona, H., Septier, F., Armand, P., Delignon, Y., Olry, C., Albergel, A., and Moussafir, J.: An adaptive Bayesian inference
722 algorithm to estimate the parameters of a hazardous atmospheric release, *Atmos. Environ.*, 122, 748–762,
723 <https://doi.org/10.1016/j.atmosenv.2015.10.026>, 2015.

724 Rojas-Palma, C., Aage, H. K., Astrup, P., Bargholz, K., Drews, M., Jørgensen, H. E., Korsbech, U., Lauritzen, B.,
725 Mikkelsen, T., Thykier-Nielsen, S., and Van Ammel, R.: Experimental evaluation of gamma fluence-rate predictions from
726 argon-41 releases to the atmosphere over a nuclear research reactor site, *Radiat. Prot. Dosimetry*, 108, 161–168,
727 <https://doi.org/10.1093/rpd/nch020>, 2004.

728 Saunier, O., Didier, D., Mathieu, A., Masson, O., and Dumont Le Brazidec, J.: Atmospheric modeling and source
729 reconstruction of radioactive ruthenium from an undeclared major release in 2017, *Proc. Natl. Acad. Sci. U. S. A.*, 116,
730 24991–25000, <https://doi.org/10.1073/pnas.1907823116>, 2019.

731 Senocak, I.: Application of a Bayesian inference method to reconstruct short-range atmospheric dispersion events, *AIP Conf.*
732 *Proc.*, 1305, 250–257, <https://doi.org/10.1063/1.3573624>, 2010.

733 Senocak, I., Hengartner, N. W., Short, M. B., and Daniel, W. B.: Stochastic event reconstruction of atmospheric contaminant
734 dispersion using Bayesian inference, *Atmos. Environ.*, 42, 7718–7727, <https://doi.org/10.1016/j.atmosenv.2008.05.024>,
735 2008.

736 Thykier-Nielsen, S., Deme, S., and Mikkelsen, T.: Description of the atmospheric dispersion module RIMPUFF, *Riso Natl.*
737 *Lab. PO Box*, 49, 1999.

738 Tomas, J. M., Peereboom, V., Kloosterman, A., and van Dijk, A.: Detection of radioactivity of unknown origin: Protective
739 actions based on inverse modelling, *J. Environ. Radioact.*, 235–236, 106643, <https://doi.org/10.1016/j.jenvrad.2021.106643>,
740 2021.

741 Ulimoen, M. and Klein, H.: Localisation of atmospheric release of radioisotopes using inverse methods and footprints of
742 receptors as sources, *J. Hazard. Mater.*, 451, <https://doi.org/10.1016/j.jhazmat.2023.131156>, 2023.

743 Wang, Y., Huang, H., Huang, L., and Ristic, B.: Evaluation of Bayesian source estimation methods with Prairie Grass
744 observations and Gaussian plume model: A comparison of likelihood functions and distance measures, *Atmos. Environ.*,
745 152, 519–530, <https://doi.org/10.1016/j.atmosenv.2017.01.014>, 2017.

746 Witte, R. S. and Witte, J. S.: *Statistics*, 496 pp., 2017.

747 Xue, F., Li, X., and Zhang, W.: Bayesian identification of a single tracer source in an urban-like environment using a
748 deterministic approach, *Atmos. Environ.*, 164, 128–138, <https://doi.org/10.1016/j.atmosenv.2017.05.046>, 2017a.

749 Xue, F., Li, X., Ooka, R., Kikumoto, H., and Zhang, W.: Turbulent Schmidt number for source term estimation using
750 Bayesian inference, *Build. Environ.*, 125, 414–422, <https://doi.org/10.1016/j.buildenv.2017.09.012>, 2017b.

751 Yee, E.: Automated computational inference engine for Bayesian source reconstruction: application to some detections/non-
752 detections made in the CTBT international monitoring system, *Appl. Math. Sci.*, 11, 1581–1618,
753 <https://doi.org/10.12988/ams.2017.74149>, 2017.

754 Yee, E., Lien, F. S., Keats, A., and D'Amours, R.: Bayesian inversion of concentration data: Source reconstruction in the
755 adjoint representation of atmospheric diffusion, *J. Wind Eng. Ind. Aerodyn.*, 96, 1805–1816,
756 <https://doi.org/10.1016/j.jweia.2008.02.024>, 2008.

757 Zhao, Y., Liu, Y., Wang, L., Cheng, J., Wang, S., and Li, Q.: Source Reconstruction of Atmospheric Releases by Bayesian
758 Inference and the Backward Atmospheric Dispersion Model: An Application to ETEX-I Data, *Sci. Technol. Nucl. Install.*,
759 2021, <https://doi.org/10.1155/2021/5558825>, 2021.

760 Zhuang, S., Fang, S., Goto, D., Dong, X., Xu, Y., and Sheng, L.: Model behavior regarding in- and below-cloud ^{137}Cs wet
761 scavenging following the Fukushima accident using 1-km-resolution meteorological field data, *Sci. Total Environ.*, 872,
762 <https://doi.org/10.1016/j.scitotenv.2023.162165>, 2023.

763